Entrainment and Decoupling Relations for Cloudy Boundary Layers

D. C. LEWELLEN AND W. S. LEWELLEN

West Virginia University, Morgantown, West Virginia

(Manuscript received 19 June 2001, in final form 29 April 2002)

ABSTRACT

An idealized model of the relationship between entrainment in cloud-topped boundary layers, circulation structure, and the degree of decoupling between the cloud and subcloud layers is developed based on simple turbulent flux distributions and the premise that the entrainment rate, both at cloud top and across cloud base when some stability exists there, is controlled by the large-eddy structure for quasi-steady buoyantly driven conditions. Layers are classified in three regimes depending on whether the cloud-top entrainment rate is ultimately limited by the transport of eddies spanning the full boundary layer (I), the cloud layer (II), or the subcloud layer (III). Algebraic relations are derived for the boundaries between, and entrainment fluxes in, each regime as a function of a convenient set of physical input parameters. The transition from regime II into III, representing the decoupling transition leading to a cumulus coupled layer, is emphasized. The model predicts that decoupling is promoted by a decrease in Bowen ratio or increase in cloud-top humidity to temperature jump ratio, and, depending on the point in parameter space, either promoted or inhibited by an increase in cloud-top radiative cooling or an increase in cloud depth. In spite of the complex cloud-layer dynamics involving cumulus plumes, a simple prediction is given for the quasi-steady cloud-top entrainment rate in regime III based on the subcloud dynamics. The model is compared with results from an extensive set of large-eddy simulations varying surface heat and moisture fluxes, cloud-top humidity and temperature jumps, and relative cloud depth. Good agreement is found with the predicted entrainment rates, the qualitative layer structure, and location of the decoupling boundary in the parameter space varied.

1. Introduction

One of the great challenges in studying cloud-topped boundary layers (CTBLs) is the range of dynamics encountered. This is true even if we set aside stable or precipitating layers or those with dynamics driven dominantly by shear, and concentrate on buoyantly driven layers, as we will in the present work. Different circulation structures occur, for example, eddies spanning the full boundary layer depth driven by a surface heat flux or cloud-top radiative cooling, or the cumulus coupled state with a distinct cloud circulation overlying a subcloud one. Ideally we would like not only a successful parameterization for turbulent fluxes, entrainment rates, cloud fractions, etc., in each dynamical regime, but also to establish, for suitably specified boundary conditions, into which regime the system is likely to organize itself. Our aim here is to make progress on a subset of these goals: to provide better cloud-top entrainment relations in some regimes and a more quantitative prediction for, and understanding of, the location in parameter space of the ''decoupling'' transition leading to the cumulus coupled state. These could prove useful, for example, in large-scale weather models where quite different parameterizations are used for different boundary layer regimes and some algorithm must be formulated to choose between them (e.g., Lock et al. 2000).

Many mechanisms for layer decoupling have been discussed in the literature, such as solar heating within the cloud layer or evaporation of drizzle below cloud base. We restrict our attention here to the case where decoupling, if present, is a consequence of heat and moisture fluxes alone. This mechanism has received attention in recent years as an important element in the stratocumulus to trade wind cumulus transition. Two-dimensional simulations of a stratocumulus-topped boundary layer (SCTBL) advecting over increasing sea surface temperatures (Krueger et al. 1995; Wyant et al. 1997) produce both a transition to trade wind cumulus and the decoupling that occurs during the process. The results, at least at a qualitative level, agree with observations of these regimes (e.g., de Roode and Duynkerke 1997). The chief role of the increasing sea surface temperature is to increase the relative importance of the surface latent heat flux. Lewellen et al. (1996) used large-eddy simulations (LESs) with prescribed surface fluxes to demonstrate that this, by itself, can lead to decoupling. Bretherton and Wyant (1997, hereafter referred to as BW97) have given the most complete dy-

Corresponding author address: D. C. Lewellen, MAE Dept. P.O. Box 6106, WVU, Morgantown, WV 26506-6106.
E-mail: dclewellen@mail.wvu.edu.

namical explanation of what they refer to as ''deepening-warming decoupling.'' They propose a diagnostic criterion for when this decoupling occurs, based on a threshold ratio of negative to positive buoyancy flux [following Turton and Nicholls (1987) in their study of diurnal decoupling]. In addition, by assuming a cloud-top entrainment parameterization and applying this to cases where cloud-top cooling and a surface latent heat flux drive the dynamics, they recast this diagnostic criterion into a predictive one based on the ratio of strengths of the two forcings. More recently, Stevens (2000) used some idealized LES to test the suitability of a version of BW97's diagnostic decoupling criterion; BW97's second criterion was not addressed because cloud-top entrainment was not included directly in the simulations.

In BW97 the authors argue that decoupling will occur if a negative buoyancy flux below cloud base would be required for the layer to remain coupled and this negative flux becomes in some sense too large for the circulation to sustain. As they stress, cloud-top entrainment plays a critical role in this picture of decoupling: entrainment warming is ultimately the source of the negative buoyancy flux appearing below cloud base. Moreover, at least within a mixed-layer model, while most features of the evolution are fairly insensitive to the closure assumption made for the cloud-top entrainment, the location of the decoupling transition depends critically on it.

It is not only that the cloud-top entrainment rate can critically affect the circulation structure. In previous work (Lewellen and Lewellen 1998, 2000) we argued a complementary result: that in many situations the boundary-layer-scale eddy structure is in turn directly responsible for determining the cloud-top entrainment rate. In Lewellen and Lewellen (1998, hereafter LL98) we argued that in quasi-steady, buoyantly driven boundary layers with the inversion layer thickness small relative to the layer depth (i.e., ''tightly capped''), the average entrainment fluxes through the capping inversion will equilibrate to the maximum levels that the large-scale eddies can transport through the full depth of the layer. In this picture the mean entrainment rate is a property of the large-scale circulation, independent of the details of the small-scale dynamics within the inversion. We defined a large-eddy entrainment efficiency for this maximum transport that is closely related to the entrainment parameterization of Stage and Businger (1981). In Lewellen and Lewellen (2000, hereafter LL00)[1] we extended these results to weakly capped layers (with or without shear across the inversion) and to entrainment across an inversion separating two buoyantly driven mixed layers. We also presented an additional result that we will make use of here: there exists a regime of enhanced large-eddy entrainment efficiency, achieved in LL00 with nonuniform surface heating arranged in separated spots.

In this work we combine aspects of the treatments in BW97 and LL98 to categorize quasi-steady CTBLs under different forcing conditions. Predicted cloud-top entrainment rates follow from the basic layer circulation structure assumed and decoupling itself is treated as an entrainment problem, circumventing the need to define a special-purpose criterion for diagnosing decoupling. In section 2 we define three idealized regimes of large-eddy entrainment behavior depending on whether the quasi-steady entrainment rate across the layer top is limited by a circulation extending across the full boundary layer depth, the cloud layer, or the subcloud layer. We derive predictions for the boundaries between these idealized regimes and entrainment rates in each as a function of a chosen set of ''input'' parameters. The transition between the last two regimes we will associate with the decoupling transition. In this analysis we concentrate on CTBLs driven dominantly by surface heat and moisture fluxes when varying those fluxes, the cloud depth, or the temperature and moisture jumps at cloud top. A more complete treatment involving cloud-top radiative cooling is given in appendix A.

We examine the applicability of this idealized picture to more realistic CTBLs in section 3 where we test the entrainment and decoupling predictions against results from a large set of numerical large-eddy simulations. LES has been used extensively in recent years to study both shallow cumulus convection (e.g., Sommeria 1976; Cuijpers and Duynkerke 1993; Siebesma and Cuijpers 1995; Grant and Brown 1999; Stevens et al. 2001) and entrainment dynamics relevant to SCTBLs (Bretherton et al. 1999; Lock 1998; Stevens and Bretherton 1999; LL98; Lock and Mac Vean 1999; van Zanten et al. 1999; Moeng et al. 1999; Moeng 2000). Such model results are necessarily not definitive. At any affordable model resolution, some smaller scales of mixing cannot be resolved and are represented instead by the effects of a subgrid model. Our philosophy here is that espoused in LL98: at least for some range of conditions the quasi-steady entrainment rate is set by the transport dynamics of large eddies, which the LES should be able to reasonably resolve. The relative insensitivity to changes in resolution of the mean statistics from simulations of shallow cumulus has also been demonstrated (Brown 1999).

2. Idealized entrainment and decoupling relations

a. Three idealized large-eddy entrainment regimes

In LL98 we argued that in a quasi-steady boundary layer large- and small-scale dynamics are both involved in transporting and mixing the entrainment fluxes throughout the layer, and will equilibrate with each other. We argued that for buoyantly driven dynamics it is natural for the small-scale processes to adjust to the

[1] It is our intent to write a full-length paper presenting these results elsewhere.

large-scale rather than vice versa, so that the large-eddy dynamics ultimately sets the mean quasi-steady entrainment rate. This allows a parameterization for the entrainment rate dependent only on features of the large-scale dynamics: a large-eddy entrainment efficiency. We approximated the large-eddy entrainment efficiency in the form

$$\eta \approx \int (\overline{w'\theta'_{v\mathrm{NE}}} - \overline{w'\theta'_v})\, dz \Big/ \int \overline{w'\theta'_{v\mathrm{NE}}}\, dz, \quad (1)$$

where $\overline{w'\theta'_v}$ is the actual buoyancy flux profile in the layer and $\overline{w'\theta'_{v\mathrm{NE}}}$ is the buoyancy flux that would result if the entrainment process being considered were not present. Note that the argument used is not ''entrainment rate is set by small scale turbulence which is driven by large-scale circulations so parameterization in terms of large scales is possible'' but that the quasi-steady entrainment rate realized is in fact the maximum one that the large-scale circulation itself can support (regardless of whether the small-scale transport at the inversion were increased or not) making the entrainment rate a property of the large-scale circulation. Both the underlying large-eddy entrainment premise and the parameterization for it were tested extensively using LES in LL98 and LL00.

In LL98 we concentrated on boundary layers in which the dominant eddy scale was the full-layer depth [so that the integration limits in (1) span the full layer]. The negatively buoyant parcels entrained at cloud top are transported across the full layer (mixing along the way) by the full-layer-scale eddies. This requires work on the part of those eddies, and the quasi-steady entrainment rate is postulated to be that which requires the maximum work that these eddies can support. That such a large-eddy entrainment limit exists is clear; that the actual entrainment rate reaches such a limit in many regimes was argued in LL98, and is taken as the working hypothesis throughout the present work.

In a cloudy boundary layer there is another idealized circulation structure that one can consider, illustrated schematically in Fig. 1. Here we view the large-eddy entrainment process as taking place in two steps. Parcels entrained at cloud top that would find their way to the surface are first transported to a layer separation height z_t by cloud-scale eddies driven by latent heat release, and from there transported the remaining distance to the surface by subcloud eddies driven by a surface flux. In quasi-steady state the upper and lower circulations will equilibrate, with the stronger one weakened as described below; this defines two regimes (with Fig. 1 illustrating the boundary in between) depending on which circulation is the weaker, limiting link in the large-eddy entrainment transport process. The three idealized large-eddy entrainment regimes identified form the basis for the subsequent theoretical analysis and comparison with LES data. For convenience we number these as I, II, and III, depending on which eddy scale primarily governs the quasi-steady, cloud-top entrainment rate: the full boundary layer scale, cloud-scale, or subcloud-scale circulations, respectively.

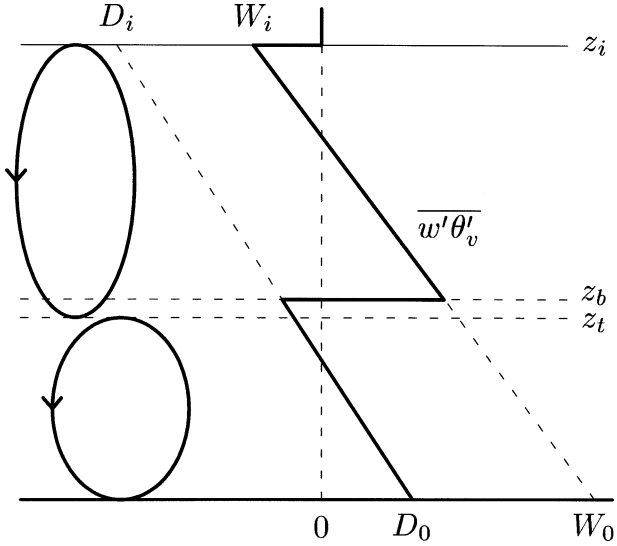

FIG. 1. Schematic circulation structure and buoyancy flux profile (solid line) for an idealized cloudy boundary layer near the regime II–III boundary. Light dashed lines are added for convenience to clarify the geometry.

We can compute an entrainment efficiency for each of the three limiting circulations by defining the no-entrainment flux and integration limits in (1) appropriately. We should also consider the possible effects of different types of eddies. As discussed in LL98, the large-eddy entrainment efficiency need not be universal; different eddy structures could give different efficiencies. For simplicity, we consider only two distinct eddy types here. This is motivated by the results of a series of LES (discussed briefly in LL00) of dry boundary layers with different superpositions of uniform surface heating and heating located in spots, varying both the spot separations and area coverage in different simulations. Rather than producing a continuum of entrainment efficiencies, these simulated convective layers tended to equilibrate into one of two distinct states: one behaving like a CBL driven by uniform surface heating, with a fairly well-mixed layer and entrainment efficiency near 0.3, and one with the dominant eddy structure being narrow updraft plumes surrounded by a weakly stable subsiding background, with entrainment efficiency near 0.6. We will assume that the full-layer-scale eddies of regime I and the subcloud eddies of regimes II and III exhibit the former behavior, while the in-cloud circulation in regime II or III exhibits the latter.[2]

To clarify the distinction between regimes II and III, consider the configuration of Fig. 1 in more detail. We

[2] A third regime with entrainment efficiency near 0.45 was encountered for surface heating arranged in fixed stripes, with no direct analog in the present study.

have assumed a quasi-steady state with linear mean fluxes of the conserved variables liquid potential temperature (θ_l) and total water (q_t), a uniform cloud base at height z_b, and a piecewise linear buoyancy flux. The latter condition is a good approximation given the other assumptions: following Sommeria and Deardorff (1977) we can express $\overline{w'\theta'_v}$ approximately (linearizing the saturation formula) as a linear combination of conserved fluxes for regions which are all cloudy or all clear:

$$\overline{w'\theta'_v} \approx \begin{cases} \overline{w'\theta'_l} + L/c_p X_2^d \overline{w'q'_t} \equiv D & \text{if } z < z_b \\ X_1^w \overline{w'\theta'_l} + L/c_p X_2^w \overline{w'q'_t} \equiv W & \text{if } z_b < z < z_i. \end{cases} \tag{2}$$

The Xs are in principle weak functions of z and temperature differences within the layer; we approximate them as constants for any given case. Typical values for stratocumulus regimes are $X_1^w \approx 0.5$, $X_2^d \approx 0.074$, and $X_2^w \approx 0.39$. The linearized ''dry'' and ''wet'' buoyancy fluxes D and W have been defined for later convenience.

The idealized picture illustrated is on the boundary between regimes II and III. The entrainment flux W_i at cloud top is transported and mixed across the full boundary layer by two distinct circulations. The upper, driven by the buoyancy flux W_b at cloud base, is just able to provide the work required to transport the negative buoyancy to the layer separation height z_t. The lower, driven by the surface flux D_0 and capped by some degree of stability at z_t, is just able to transport the negative buoyancy flux D_t across the subcloud layer. Note that the height z_t lies below the height z_b. This is a manifestation of a third entrainment process at work. The upper circulation entrains from below across the level z_t as well as from above across z_i, again with the magnitude of the entrainment postulated to be the maximum that the upper circulation can support. In the large-eddy entrainment picture, we need not detail the processes that may be occurring around z_t (e.g., distinguishing between small-scale turbulent mixing or penetrating up- or downdrafts); all that matters is how these flux contributions affect the large-scale circulations. In the quasi-steady state the rate will ultimately equilibrate to the maximum the circulations can support regardless of the precise mix of events occurring at z_t.

In Fig. 1, the entrainment dynamics of the two circulations are just balanced so that the conserved fluxes across the full layer are approximately linear and the dynamics are quasi steady. What happens when we move off the II–III boundary in either direction? Consider, for example, an increase in W_0 but not D_0. This will increase the in-cloud circulation and raise the entrainment rate at cloud top. The subcloud circulation, which was not augmented by the change, cannot transport the additional negative buoyancy flux through the subcloud layer. A transitional period ensues in which the upper layer heats and dries at a faster rate than the subcloud layer. This builds up the stable layer at z_t and perhaps drives that layer downward as well. As the temperature and humidity gradients at z_t increase, the plumes crossing this boundary become increasingly more moist and cold relative to the background in the upper layer, which leads to the formation of column clouds. This helps to restore the balance between the upper and lower circulations in two ways: it can lower z_t (making the subcloud circulation's job in the entrainment flux transport easier), or raise the main cloud base z_b (reducing the buoyancy flux driving the upper circulation). Eventually a new balance is achieved with linear conserved fluxes across the full layer, the upper layer only partly cloudy due to the presence of the cumulus cloud columns, and the subcloud circulation entraining at the maximum rate the given surface flux can support. We define this as regime III.

Consider the reverse process. Beginning with a state in regime III, either increase D_0 or decrease W_0. This favors the lower circulation over the upper, and a transitional period follows in which the subcloud layer heats and dries faster than the upper layer. This in turn weakens the cap at z_t as well as forcing it upward, reducing the column clouds. With a sufficiently large change in D_0 or W_0 the column clouds disappear and the stable layer at z_t is weakened enough that a significant portion of the subcloud circulation passes through, reducing the subcloud circulation and augmenting the in-cloud one. The new quasi-steady state achieved has the subcloud entrainment below the maximal level that could be driven by the given surface flux, and the cloud-top entrainment rate at the maximum that the upper circulation can support. We define this as regime II.

Away from the II–III boundary, additional information is required to compute η for the ''nonlimiting'' circulations (for the upper circulation in III, a model for the buoyancy flux in terms of the conserved fluxes when conditions are partly cloudy; for the lower circulation in II, a measure of how much of the circulation is capped). But, assuming the upper and lower circulations have equilibrated, it is not necessary to compute these efficiencies for the analysis below; computing the entrainment rate for the simpler ''limiting'' circulation is enough.

To summarize the regime definitions: if we denote the large-eddy entrainment limits, which can be supported by the full-layer-scale, cloud-scale, and subcloud-scale eddies as $\mathrm{ENT}^{(\mathrm{I})}$, $\mathrm{ENT}^{(\mathrm{II})}$, and $\mathrm{ENT}^{(\mathrm{III})}$, respectively (where the cloud-scale result is considered for a solid cloud deck), then the regimes are determined according to

$$\begin{aligned} &\mathrm{ENT}^{(\mathrm{II})} < \mathrm{ENT}^{(\mathrm{I})} && \text{for regime I,} \\ &\mathrm{ENT}^{(\mathrm{I})} < \mathrm{ENT}^{(\mathrm{II})} < \mathrm{ENT}^{(\mathrm{III})} && \text{for regime II, and} \\ &\mathrm{ENT}^{(\mathrm{III})} < \mathrm{ENT}^{(\mathrm{II})} && \text{for regime III.} \end{aligned} \tag{3}$$

It remains to relate each idealized regime to physically observed boundary layers. The dry convective boundary layer (CBL) driven by a surface sensible heat flux and the typical SCTBL driven by cloud-top radiative cooling are generally well mixed, with pdf's of

dynamic variables relatively Gaussian. We associate these with regime I. Shallow cumulus layers with their column-cloud structure (with or without a layer of horizontally uniform clouds at the top), more narrow plumes in the cloud layer surrounded by a weakly stable, slowly subsiding background flow, and subcloud layer behaving like a CBL capped at cloud base (see, e.g., Garstang and Betts 1974; Sommeria 1976), we naturally associate with regime III. The expected signatures of regime II lie in between those of I and III with skewed dynamics in the cloud without a completely capped subcloud layer. The natural candidates are then what might be classified as SCTBLs, with an approximately horizontally uniform cloud cover, but with a more pronounced contribution of the surface latent heat flux to the dynamics giving rise to more organized updrafts within the cloud, and slightly less well-mixed thermodynamic profiles with some weak stability at cloud base (restricting some circulations to the subcloud layer). For our purposes, the most important distinction between regime II and I is the higher cloud-top entrainment rate. The description of the transition from a stratus-topped boundary layer (STBL) to a trade cumulus boundary layer (TCBL) given in Krueger et al. (1995) identifies two intermediate stages, the deep stratus-topped boundary layer (DSTBL) and cumulus-under-stratocumulus boundary layer (CUSBL). Based on their descriptions we would tentatively identify their STBL as in regime I, DSTBL in II, and CUSBL and TCBL in III.

Obviously, when applied to real cloudy boundary layers the regimes we have described are idealizations. One could attempt to refine the picture by considering composite eddy structures or different admixtures of full-scale, cloud-scale, and subcloud-scale eddies. These might well be more accurate physical representations of the actual layers (particularly near the I–II boundary as noted below), but here we wish to test the validity of the basic physical picture in its simplest version. The extent to which the idealized regimes are applicable to more realistic layers is ultimately most directly tested by how well the entrainment rates themselves are predicted. These, along with more qualitative expectations, will be examined in section 3 using LES data.

Crossing the boundary between regimes II and III, which we associate with the decoupling transition leading to a cumulus coupled state, is a continuous process as we have described it. States on the boundary simultaneously exhibit the behavior expected in each regime (albeit with only a short column cloud in III). This is not true of the boundary between I and II, where the idealized circulation structure changes discontinuously. It is likely that a continuum of admixtures of full-layer and in-cloud-layer circulations will be encountered in real cloudy layers between the two idealized limits. Nonetheless, there is a feedback effect that sharpens the boundary between the two limits by driving the system towards one or the other. Entrainment promotes the regime II eddy structure in the cloud layer by stabilizing the background flow around the updraft plumes through warming and drying. Therefore, if regime II behavior would lead to the larger entrainment at cloud top, then a perturbation towards regime II behavior leads to increased entrainment, which in turn promotes regime II behavior. If regime I behavior leads to larger entrainment, then an increase in regime II behavior leads to decreased entrainment, which then inhibits regime II behavior. In either case the feedback tends to drive the system toward the appropriate idealized regime behavior.

b. An idealized set of boundary layers

For any given set of physical conditions we can in principle compute three different possible large-eddy entrainment rates, one for each of our idealized circulation regimes, using (1) and assumed entrainment efficiencies. Comparing the results with our schematic regime definition (3) allows one to predict which regime the system should be in and what the entrainment rate is. In certain limits we can carry out this program analytically and thereby map out the predicted ''phase space'' of layer behaviors as a function of suitably chosen control parameters. For this purpose we make the following simplifying assumptions.

1) The layer is tightly capped so that the inversion height (z_i) is determined without ambiguity, and the mean vertical profiles of θ_l, q_t, and their fluxes have discrete jumps at z_i.
2) The layer is driven solely by some specified combination of surface heat and moisture fluxes ($\overline{w'\theta'_{l0}}$ and $\overline{w'q'_{t0}}$), leaving out any radiative heating or cooling, mean wind shear, precipitation, etc.
3) The cloud deck is horizontally uniform. This allows the buoyancy flux to be approximated as in (2). This restriction can be reasonably enforced in regime III only near the boundary with II (where the column clouds are not yet significant), but this is sufficient for our purposes of locating the regime boundaries and computing the expected entrainment rate.
4) The layer dynamics are quasi-steady in the sense that the surface fluxes, inversion properties, cloud thickness, and shapes of the mean θ_l and q_t profiles are changing on timescales that are much longer than the timescales of the boundary layer circulations. This means in particular that the conserved fluxes $\overline{w'\theta'_l}$ and $\overline{w'q'_t}$ are to a good approximation linear for $z < z_i$. (Note that this approximate linearity does not require the layer to be well mixed.)

Nondimensionalizing our problem with the above restrictions results in a three-dimensional physical parameter space. For coordinates in this space we choose a convenient set of what can fairly be considered input parameters: the normalized height of the top of the subcloud layer $\hat{z}_t \equiv z_t/z_i$ (or sometimes the nondimensionalized cloud base height $\hat{z}_b \equiv z_b/z_i$) and the ratios of the dry and wet buoyancy fluxes at the surface and at

z_i. For our conditions the latter are related to the more familiar surface Bowen ratio $B \equiv (c_p/L)\overline{w'\theta'_{l0}}/\overline{w'q'_{t0}}$ and cloud-top jump ratio $\zeta \equiv (-L/c_p)\Delta q_t/\Delta\theta_l$, by

$$D_0/W_0 = (B + X_2^d)/(X_1^w B + X_2^w) \quad (4)$$

$$W_i/D_i = (X_1^w - X_2^w\zeta)/(1 - X_2^d\zeta). \quad (5)$$

Note that while the entrainment fluxes $\overline{w'q'_{ti}}$ and $\overline{w'\theta'_{li}}$ are unknown a priori, their ratio is not: for our idealized conditions this is simply equal to the jump ratio $\Delta q_t/\Delta\theta_l$. This is no longer the case when cloud-top radiative cooling is included, complicating the resulting formulas (cf. appendix A).

When $W_i/D_i < 0$ (or, for typical conditions, $\zeta \gtrsim 1.3$) the solid cloud-top becomes nominally evaporatively unstable via the cloud-top entrainment instability (CTEI; Randall 1980; Deardorff 1980). For our conditions this situation is inherently unsteady: entrainment produces a positive buoyancy flux and so will rapidly increase until something (generally a partial reduction of the cloud cover) changes to allow a quasi-steady equilibrium to be achieved. Our analysis holds then for this end point. Some of our LES examples in section 3 fit into this category: layers ending up in regime III with $W_i > 0$, but with only a partial cloud cover at the top of the layer so that the entrainment process again represents a net energetic cost.[3]

It is not essential that assumptions 1–4 be satisfied exactly; in practice the results prove applicable for much weaker conditions. As shown in LL00, the entrainment efficiency in a buoyantly driven layer is insensitive to the capping strength, and mean shear across the inversion can be included without altering the discussion as long as the production of turbulent kinetic energy due to that shear is small compared to the buoyant production. The most serious restriction in assumption 2 is that of no cloud-top cooling; we restore this ingredient in appendix A. We have set it aside here because including it effectively increases the parameter space we have to consider from three dimensions to five. A quasi-steady assumption is essential at some level. When the θ_l and q_t profiles change their shapes due to turbulent mixing at a significant rate, the different scales of flux transport need not be in equilibrium with one another and a single rate is insufficient to parameterize the entrainment. Nonetheless, there are both weaker and stronger versions of assumption 4 worth considering, which will be discussed briefly later on.

[3] It is easy to end up in regime I as well, with little or no cloud, but in this picture there are no quasi-steady states with $W_i > 0$ in regime II. The cloud cover being partial forces the cloud layer either to be thin (implying regime I) or to consist of column clouds. The latter requires buoyancy differences large compared to those between different parcels in the subcloud layer, which in turn implies sufficient capping to the subcloud layer to ensure that the subcloud circulation is entraining maximally and the system is then in regime III. This is one reason why, in determining our regime boundaries, we can avoid treating partly cloudy conditions for the upper circulation.

Approximately linear conserved flux profiles prove convenient for analytically deriving simple relations, but are not required for the basic treatment to be followed. If the forcings from radiation, large-scale horizontal advection, subsidence,[4] precipitation, etc. are assumed known, then the total effective fluxes including these contributions are again linear, so W and D are still determined (though with more complex shapes) up to a single parameter, which can be taken as the cloud-top entrainment rate. At the cost of increased complexity, the entrainment efficiencies in each regime can then still be computed from (1), and the predicted regimes and entrainment rate established from (3).

Note that our entire analysis is conducted at the level of the mean flux profiles. The temperature and humidity profiles are not used directly, and we do not need to assume any specific idealized structure for them. Our results will be limited to entrainment rates, regime boundaries, and qualitative features; we are not providing a complete mixed layer model or predicting the detailed evolution of the thermodynamic profiles in any model limit.

c. *Predicted entrainment rates and regime boundaries*

With our assumptions we encounter flux profiles such as in Fig. 1. To apply the large-eddy entrainment conditions using (1) we must appropriately identify the buoyancy fluxes and ''no-entrainment'' buoyancy fluxes for each process. These are shown schematically in Fig. 2. The efficiencies for the entrainment into the subcloud layer appropriate for a regime III circulation (η_{sc}); into the cloud layer from cloud-top (η_c) and from the subcloud layer below (η_b) appropriate for a regime II circulation; and into the layer across cloud-top appropriate for a regime I full-layer circulation (η_f) are, accordingly,

$$\eta_{sc} = -D_t/D_0 \quad (6)$$

$$\eta_c = -W_i/W_b \quad (7)$$

$$\eta_b = \frac{(1 - \hat{z}_b)(W_t - W_b) - (\hat{z}_b - \hat{z}_t)(D_b + D_t)}{(1 - \hat{z}_b)(W_t + W_i)} \quad (8)$$

$$\eta_f = -\frac{\hat{z}_b^2 D_i + (1 - \hat{z}_b^2)W_i}{(1 - \hat{z}_b)^2(W_0 - D_0) + D_0}. \quad (9)$$

The entrainment process described by (8) is (though flipped upside down) closely analogous to the radiatively cooled cases in LL98 with the cooling height dropped below the inversion height. A case with en-

[4] Subsidence at reasonable levels will lead to significant deviations from linear flux profiles only when the gradients in the associated conserved variable are large, which we expect only deep in regime III. So it will not significantly affect the position of the II–III boundary or entrainment predictions for regimes I and II derived below, but needs to be accounted for in the entrainment prediction when long column clouds are present.

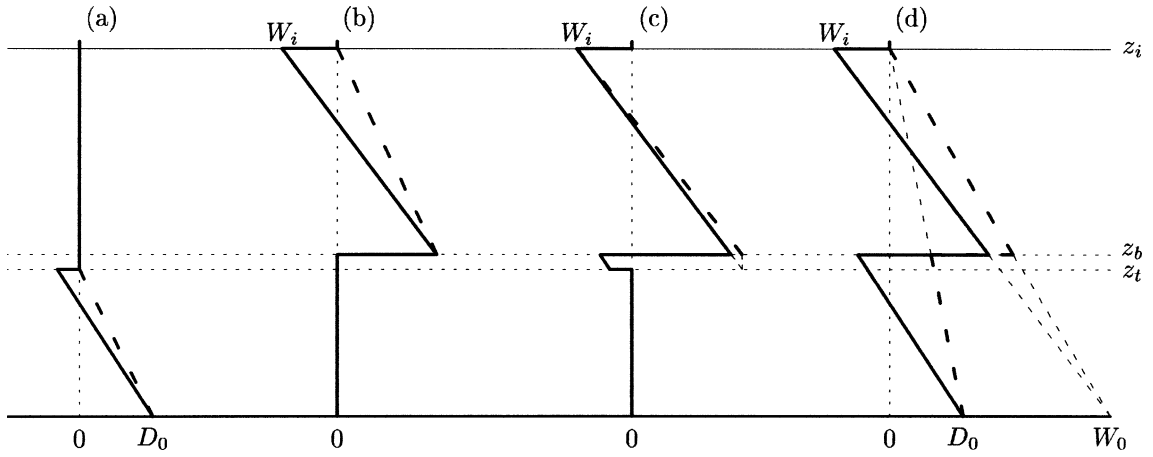

FIG. 2. Schematic buoyancy fluxes (solid line) and no-entrainment buoyancy fluxes (heavy dash) used in computing large-eddy entrainment efficiencies for different circulations and entrainment processes as described in the text: (a) η_{sc}, (b) η_c, (c) η_b, and (d) η_f.

trainment into both the top and the bottom of a layer was considered in LL98 as well. The other efficiencies are computed exactly as in LL98. In computing η_b and η_c we have ignored any contribution of the subcloud plumes to the vertical momentum of the cloud plumes; this may be less justified near the regime I boundary.

Using the linearity of the D and W profiles, we can solve these relations for the entrainment fluxes predicted for each circulation regime:

$$D_i^{(\mathrm{III})} = D_0[1 - (1 + \eta_{sc})/\hat{z}_t] \tag{10}$$

$$D_i^{(\mathrm{II})} = (D_i/W_i)W_0(\hat{z}_b - 1)/(\hat{z}_b + 1/\eta_c) \tag{11}$$

$$D_i^{(\mathrm{I})} = -\eta_f D_0 \frac{(1 - \hat{z}_b)^2(W_0/D_0 - 1) + 1}{(1 - \hat{z}_b^2)(W_i/D_i) + \hat{z}_b^2}. \tag{12}$$

The superscripts label which regimes the entrainment predictions should be appropriate for. The corresponding wet entrainment buoyancy fluxes are obtained from these by multiplying by (W_i/D_i).

Plugging these into the regime definition (3) then provides the regime predictions

$$|D_i^{(\mathrm{II})}| < |D_i^{(\mathrm{I})}| \quad \text{for regime I} \tag{13}$$

$$|D_i^{(\mathrm{I})}| < |D_i^{(\mathrm{II})}| < |D_i^{(\mathrm{III})}| \quad \text{for regime II} \tag{14}$$

$$|D_i^{(\mathrm{III})}| < |D_i^{(\mathrm{II})}| \quad \text{for regime III.} \tag{15}$$

This specifies the I–II boundary in about as simple a usable form as we can express it [$D_i^{(\mathrm{I})} = D_i^{(\mathrm{II})}$]. There is work yet to be done on the more interesting II–III decoupling boundary [$D_i^{(\mathrm{II})} = D_i^{(\mathrm{III})}$], however, because (10) is expressed in terms of $\hat{z}_t$ but (11) in terms of $\hat{z}_b$. It is straightforward to use the extra entrainment relation (8) to eliminate $\hat{z}_b$, but rather messy. The resulting equation for the decoupling boundary, which proves too complicated to be very edifying, is plotted for a range of values of W_i/D_i in appendix A. We can cast the result in a much simpler form if in regime II we assume that W_b/W_t is approximately constant; we use the full solution to justify this approximation, a posteriori, with a value of 0.9 chosen for the ratio. In this approximation, (11) becomes

$$D_i^{(\mathrm{II})} = (D_i/W_i)W_0(\hat{z}_t - 1)/(\hat{z}_t + 1/\tilde{\eta}_c), \tag{16}$$

where

$$\tilde{\eta}_c \equiv -W_i/W_t \approx 0.9\eta_c. \tag{17}$$

Now, using (10) and (16) in the regime III condition (15), and rearranging gives the following form for the decoupling boundary:

$$\frac{D_0}{W_0}\frac{W_i}{D_i} \le \frac{\hat{z}_t(1 - \hat{z}_t)}{(\hat{z}_t + 1/\tilde{\eta}_c)(1 + \eta_{sc} - \hat{z}_t)} \quad \text{for decoupling.} \tag{18}$$

A priori, we would have expected the boundary to be a complicated surface in the three-dimensional space of control parameters $\hat{z}_t$, D_0/W_0, and W_i/D_i, but in the present approximation the latter two occur only in the simple product, leaving the boundary effectively as a line in a two-dimensional space. This result is compared to the full solution in appendix A, demonstrating that the approximation resulting from using (16) in place of (11) is indeed a good one. The appendix also presents the analog of (18) when cloud-top radiative cooling is included.

We are assuming that the entrainment efficiencies are known quantities. As noted previously we will use values found for dry convective boundary layers in two limits: uniform surface heating, and heating in widely separated spots. In LL98 we reported a small decrease in η for a simulated CBL as the horizontal grid spacing is reduced,[5] with a value of $\eta = 0.29$ for the best res-

[5] The largest changes in the flow structure are found in the lower part of the boundary layer where the heat flux transitions from being carried by the subgrid modes to being carried by the resolved ones. The resulting changes in the dissipation rate there may be as much responsible for the change in η with resolution as any effects in the inversion region itself.

olution considered (cf. Fig. 9 in that work); subsequently, at higher resolution ($\Delta x = 0.026 z_i$), we have found $\eta = 0.27$, continuing this trend, and a simple extrapolation implies that the true η might be as low as 0.25. For the present work, such differences are of little consequence and we simply take $\eta_{sc} \approx 0.3$ when comparing with LES results in section 3. For η_c we choose a value of 0.55, in agreement with our spot heating simulations with the best statistics and, accordingly, a value of 0.5 for $\tilde{\eta}_c$; we will see below that this is consistent with our current results. The value of η_b is only of secondary importance, and more poorly determined by our previous simulations; we choose $\eta_b = 0.3$ as well for simplicity.

d. Further comments on regime transitions

It is easy to see that (18) is consistent with the behavior described earlier: increasing W_0 or decreasing D_0 drives the system toward regime III. The boundary between regimes II and III could also be traversed by changing the cloud-top jump conditions (W_i/D_i), or the cloud-base height ($\hat{z}_b$ or $\hat{z}_t$). Decreasing (increasing) W_i/D_i increases (decreases) the wet buoyancy flux W over the dry D, in turn increasing (decreasing) the upper circulation relative to the lower, and heating and drying the upper (lower) layer at a relatively higher rate, forcing the system toward regime III (II) as above. Decreasing the cloud-base height has two opposing effects: it makes it easier for the subcloud circulation to transport entrained fluxes to the surface, and it increases the in-cloud buoyancy flux. Which of these effects dominates depends on the cloud depth itself, with the position of the crossover point, at $\hat{z}_t \approx 0.63$, relatively insensitive to the precise values chosen for the η's. Note that the stability of a layer with respect to column cloud growth is potentially quite different depending on which side of the crossover point the system is on. On the lower (thicker cloud) side a layer in regime II will be driven further into regime II by any perturbation decreasing $\hat{z}_t$, while on the upper side it will be driven toward, and finally into, regime III where column clouds can persist and grow.

As noted earlier, we do not expect to encounter an abrupt transition in circulation structure when physically crossing the predicted I–II regime boundary. Nonetheless, the qualitative behavior of (13) is as expected. Thicker clouds or larger latent heat fluxes favor regime II; thinner clouds and larger sensible heat fluxes favor I. Note that the condition (14) for a regime II layer is almost certainly a necessary one but probably not always sufficient. In our simulations of dry layers with nonuniform surface heating we found that the spot heating type circulation giving enhanced entrainment is destroyed if a large enough admixture of uniform heating is added, or if the spots are too closely spaced. This suggests that regime II behavior may be inhibited if the system is in some sense too far from the regime III boundary, or if $\hat{z}_b/(1 - \hat{z}_b)$ is too small. Further discussion of this issue, or the effects of cloud-top radiative cooling on the I–II boundary, we defer to future work.

e. Weaker or stronger quasi-steady approximations

Decoupling is inherently tied to the formation and maintenance of a stable ''transition'' layer at z_t. Of the three entrainment processes we have considered, one, that at cloud top (η_c), tends to strengthen the transition layer, while the other two tend to erode it, one from above (η_b) the other from below (η_{sc}). In quasi-steady state (in the form of our assumption 4) approximate balances are reached between the three: between the first and the latter two so that the gradients at z_t change slowly, and between the latter two so that the height z_t itself changes slowly. Both stronger and weaker forms of the quasi-steady assumption are worth considering (and are readily encountered in LES results). If we consider a boundary layer with external conditions that would place it in regime II or III, but initialize it at some point away from its desired equilibrium, it will progress naturally through three levels of quasi steadiness as dynamical modes on longer and longer timescales have a chance to equilibrate. The individual cloud and subcloud circulations equilibrate first, providing fluxes of conserved variables that are linear across each layer but whose slopes in the two layers differ—over time this allows the gradients at z_t to build up. In time the two circulations equilibrate with each other and assumption 4 is achieved with linear conserved fluxes across the full layer. Finally, because of the critical role it plays in the dynamics, z_t is driven to a steady value if given enough time. This requires not only a balance between the entrainment processes represented by η_b and η_{sc} (which is achieved relatively quickly because any significant imbalance easily shifts z_t since the temperature difference across z_t is small), but a balance between the rates of change of cloud-base height due to the change of temperature and humidity in the layer, in turn due to turbulent fluxes, large-scale advective forcings and radiative terms (a balance that takes longer to achieve). This does not require the thermodynamic profiles themselves to be steady, although this is achievable for some conditions. In the weakest level of quasi steadiness of the three, (18) is not applicable but the individual entrainment relations (6)–(8) still are (the latter two provided that the cloud layer is still approximately horizontally uniform). Given the strongest level, (18) and equations leading to it hold and we can formulate an additional relation as well; for example,

$$\frac{dq_t/dt}{d\theta_l/dt} = \frac{(dq_t/dt)_{\mathrm{LS}} - \partial\overline{w'q_t'}/\partial z}{(d\theta_l/dt)_{\mathrm{LS}} - \partial\overline{w'\theta_l'}/\partial z} = \alpha_s \quad \text{for } z = z_c, \tag{19}$$

where α_s is the slope of the saturated humidity with changing θ_l. Solving for the entrainment fluxes as before, (19) could then be used to solve, for example, for the steady-state cloud base height. A steady state for z_t

is often efficiently approached, because a change in entrainment rate, which depends sensitively on z_t, changes the turbulent fluxes of heat and humidity by different factors.

f. Comparison with other formulations of the decoupling boundary

In our analysis decoupling is a consequence of the subcloud circulation being unable to support any additional negative buoyancy flux transport from z_t to the surface. That is, (6) is a necessary and sufficient condition for diagnosing decoupling; in this analysis it replaces the ''buoyancy integral ratio'' (BIR) threshold porposed in Turton and Nicholls (1987) and used in BW97 to diagnose the type of decoupling we are considering here:

$$\mathrm{BIR} = -\int_{z<z_{b\max},\,\overline{w'b'}<0} \overline{w'b'}\,dz \Big/ \int_{\text{all other } z} \overline{w'b'}\,dz < 0.15. \tag{20}$$

While similar in spirit, the BIR involves the buoyancy flux over the full layer, not just the subcloud portion, and involves the negative buoyancy flux generated by both the subcloud and in-cloud circulations at cloud base (described by η_{sc} and η_b here). The BIR predicted on the decoupling boundary by the present analysis is not constant, varying in particular with $\hat{z}_t$ and D_0/W_0 as the relative importance of the in-cloud and subcloud contributions to the buoyancy flux change. Another practical difference is that a BIR threshold represents a Kraus and Schaller (1978)–type entrainment measure. This is much more sensitive to horizontal averaging effects than a Stage and Businger (1981)–type measure: the negative contribution to the buoyancy flux integral is reduced or even eliminated by averaging over a horizontal variation in cloud base heights. Stevens (2000) sidesteps this difficulty by replacing the actual mean buoyancy flux in the BIR with a piecewise linear ''mixed-layer'' flux (e.g., as in Fig. 1). In his BIR definition Stevens also includes the entire negative buoyancy flux area in the numerator, not just that below cloud base as in BW97. With this definition we predict BIR values on our II–III boundary varying from just below 0.1 up to about 0.4.

Given the importance of latent heat fluxes in promoting decoupling and sensible heat fluxes in retarding it, Lewellen et al. (1996) suggested that the ratio β of the liquid water flux contribution to the buoyancy flux to the total buoyancy flux might provide a useful decoupling diagnostic. As with the BIR threshold, the measure β does not account for the effects of changing the relative importance of in-cloud and subcloud circulations. It is possible for a layer to remain coupled [according to (18)] even with large β if $\hat{z}_t$ is small, or to be decoupled even for modest values of β if $\hat{z}_t$ is large.

Our primary goal is not simply to diagnose decoupling, but to predict its occurrence in terms of parameters we might naturally take as inputs in a boundary layer model, as in (18) or its generalization including cloud-top cooling, (A4) in appendix A. This again follows BW97 to a large degree in spirit, but with notable differences in results. In their ''minimal model'' of decoupling (taking a BIR threshold of zero, and a steady state, among other assumptions) they find the condition for decoupling of a layer driven dominantly by a surface latent heat flux and radiative flux jump (ΔF_r) at cloud-top to be

$$\Delta F_r/[(L/c_p)\overline{w'q'_{t0}}] < 2.5\sigma A(1 - \hat{z}_b), \tag{21}$$

where the thermodynamic coefficient σ is approximately 0.35, and A is the coefficient appearing in their bulk-Richardson-number-based closure for cloud-top entrainment ($w_e\Delta\theta_v = 2.5Az_i^{-1}\int \overline{w'\theta'_v}\,dz$). This formula predicts that an increase in ΔF_r retards decoupling, an increase in fractional cloud depth promotes it, and there is no explicit dependence on the subcloud circulation or the cloud-top jump conditions. The situation in (18) or (A4) is more complex: the dependence of the predicted decoupling boundary on $\overline{w'\theta'_{l0}}$ and ζ are explicit, and an increase in relative cloud depth or cloud-top cooling can either promote or inhibit decoupling. Some of these features may be implicit in the more general formulation given in appendix B of BW97 [leading to their Eq. (24)] but the dependencies are not clear; that result is written in terms of the flux slopes, which implicitly depend on $\overline{w'\theta'_{l0}}$, ζ, $\hat{z}_t$, and ΔF_r.

3. Comparison with LES results

a. LES model and simulation set

The LES model used is the same as that employed in LL98, and is described there and in references therein. It is a fully three-dimensional, unsteady, finite difference implementation of the incompressible Navier–Stokes equations in the Boussinesq approximation, second-order accurate in space and time. The basic fluid dynamics implementation is given in Sykes and Henn (1989), and the cloud dynamics described in Sykes et al. (1990). Staggered grids are employed for the different field variables. The horizontal grids are uniform, but the vertical grids are stretched to allow finer grid spacing near the ground and in the region of the capping inversion. The piecewise parabolic model algorithm is used for the advection of the conserved thermodynamic variables θ_l and q_t. The subgrid model employs a quasi-equilibrium, second-order turbulence closure scheme, with the maximum turbulence length scale related to the numerical grid length and constrained near the surface and in the presence of stable stratification. A subgrid partial cloud-

iness scheme is employed following Sommeria and Deardorff (1977) and Mellor (1977), with the saturation variance carried as a prognostic variable.

The principal simulation set is summarized in Table B1 in appendix B. The conditions were chosen more for ease of analysis of the underlying physics than to maximize direct physical relevance. As discussed in the previous section we leave out precipitation, mean shear, large-scale subsidence (aside from the few exceptions noted) shortwave heating and, most significantly, longwave cloud-top cooling. Fixed surface fluxes of θ_l and q_t were specified. The horizontal domain was 3.2 km $\times$ 3.2 km, with an inversion height of approximately 750 m. The vertical grid spacing was 5 m near the surface and in the region of the capping inversion, and smoothly stretched elsewhere to a maximum of typically 20–30 m. Generally the horizontal grid spacing was 40 m; a few chosen cases were also run with $\Delta x = 20$ m. Many preliminary runs were performed with $\Delta x = 80$ m, in order to sample what is necessarily a large physical parameter space (even for our restricted conditions). Quite generally the different resolutions gave very similar results, consistent with the picture presented in LL98.

With a few exceptions we simulated tightly capped boundary layers to simplify the analysis and to permit steadier time averages. In the majority of the cases this was achieved with a device we employed for some of the simulations in LL98: a rigid lid is placed at 750 m height and a negative heat flux, larger than what can be entrained into the layer below, is forced through it. The heat flux that is not entrained collects in a thin layer underneath the lid, forming the tight capping inversion. The magnitude of the entrainment flux proves to be the same as if there were a weaker inversion cap and no lid (LL98, LL00). For present purposes this arrangement has two practical advantages: a nearly constant ratio of entrained heat to moisture flux can be maintained even for long simulations, and the number of vertical grid points needed is reduced. This procedure is similar to that employed by Stevens (2000) in his LES decoupling study, but there is an important difference. The entrainment fluxes into the cloud layer in our simulations are determined internally by the dynamics. In Stevens's cases (where they are meant to include the combined effects of entrainment and cloud-top radiative cooling) they are externally prescribed (the flux is small enough that no inversion forms under the lid); this eliminates what, for the present study, is a crucial feedback mechanism for the layer dynamics. A smaller number of our simulations included conventional inversions, with zero lapse rates above them. For most of these we again employed tight caps ($\Delta\theta_l \sim 20$ K) to keep W_i/D_i and z_i nearly constant through the course of the simulation, but in a few the initial cap is weaker and the variation of W_i/D_i becomes the principal time variation in the simulation.

Cloud thickness is one of the principal variables in this study. In order to reach nearly steady conditions for a range of cloud thicknesses in some cases, or to progressively grow or shrink the cloud thickness at controlled rates in others, we include uniform drying or cooling terms in some simulations, as listed in Table 1. In practice this proves more convenient than varying the initial temperature and humidity levels within the layer, though this could serve much the same purpose. Physically these terms may be considered as arising from advection on much larger scales than what we simulate within our domain. These are taken constant throughout the domain; imposed heating or drying with some prescribed vertical profile can directly act as a source or sink of buoyant energy, affecting the entrainment dynamics as well as making the steady-state flux profiles of the affected variables nonlinear. As noted earlier, the analysis of section 2 could be extended to include such profiles but at the cost of additional complexity.

The simulations were run long enough before any of the statistics presented here were gathered so that the details of the initial conditions are unimportant. The simulated time durations ranged from 3 to 36 h, with very steady cases on the lower end and ones progressing in time through a range of cloud conditions on the upper end. A quantitative comparison with the results of section 2 requires not only a large set of different conditions but good statistics for each. Ideally we would employ large horizontal domains so that horizontal averaging alone would include a sufficient sample of eddy structures to provide a good quasi-steady statistical average. It is numerically more efficient, however, to use more modest domains with time averaging supplementing the horizontal averaging. The results presented here are all based on 2-h averages, with the fields sampled every 20 s. For the range of conditions simulated, 1-h averages are reasonably steady, but, particularly when sampling over more intermittent cumulus plumes, the 2-h averages represent a worthwhile improvement.

b. *Different surface-driven cloudy boundary layer regimes*

Before quantitatively testing the predictions of section 2, we present sample mean vertical profiles for cases predicted to be in different regimes as support for the qualitative picture we have described. Here and throughout the subsequent data comparison we label the simulated layers at the given times according to the regimes in which the analysis of section 2 would predict they fall. That is, the identifications are based solely on the measured control parameters $\overline{w'\theta'_{l0}}$, $\overline{w'q'_{t0}}$, W_i/D_i, and $\hat{z}_b$ or $\hat{z}_t$, not on any other properties observed in the simulated results. Figure 3 shows profiles from a few simulated regime I boundary layers. Even with the large range of cloud thicknesses, we find broadly similar be-

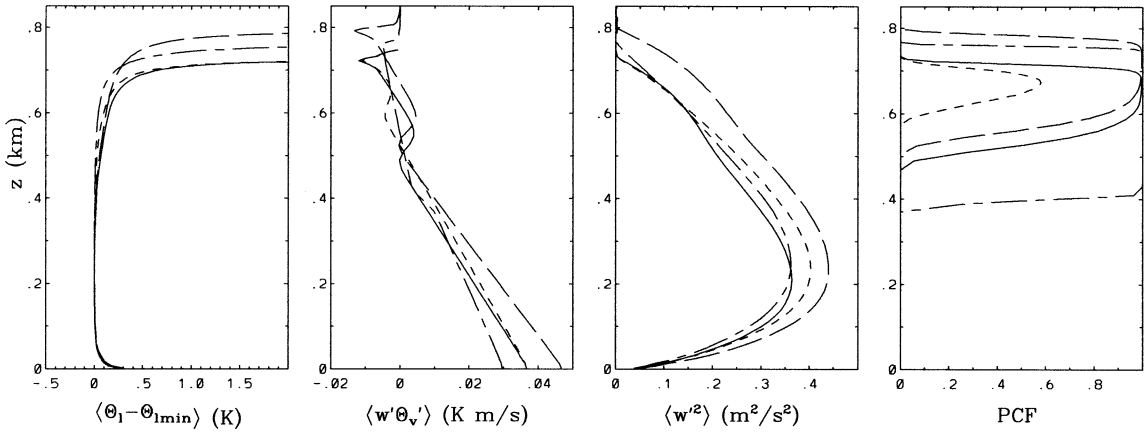

FIG. 3. Mean vertical profiles of liquid potential temperature difference, potential temperature flux, vertical velocity variance, and partial cloud fraction for selected LES cases in regime I. Runs T5 at two times (solid, and short dash), N2 (long dash), and CN (long–short) from Table 1.

havior consistent with our expectations: well-mixed thermodynamic profiles and eddy circulations similar to those in the dry CBL. The profiles in Fig. 4 are from a series of quasi-steady simulations with different $\overline{w'\theta'_{l0}}$, but other control parameters held constant or nearly so. The one shown with the largest surface sensible heat flux (run T4) is, according to (14), just across the regime I–II boundary in regime II. As $\overline{w'\theta'_{l0}}$ is decreased, the relative importance of the surface latent heat flux increases; the buoyancy flux at cloud base decreases; the circulations take on more of the character of distinct in-cloud and subcloud components (e.g., the local minimum in $\overline{w'^2}$ that appears at cloud base); gradients in q_t (not shown) and θ_l around cloud base form and gradually increase; and the vertical velocity skewness in the cloud layer (not shown) slowly increases. The simulation in Fig. 4, with the lowest $\overline{w'\theta'_{l0}}$ (run T0) is, according to (18), just across the II–III boundary in regime III. Relative to the other simulations in Figs. 3 and 4 this simulation possesses a distinct column cloud and dramatically increased θ_l and q_t gradients in the column cloud layer and skewness in the cloud layer.

Figure 5 samples the variety of profiles present in simulations that we predict to be in regime III. We find a large range of behaviors in all the horizontal mean statistics, but always the indication of a column cloud in the cloud fraction profile, distinct gradients of θ_l and q_t and large vertical velocity skewness in the cloud layer, and a distinct subcloud peak in the vertical velocity variance (characteristic of a distinct subcloud circulation). Note that the small, sharp negative buoyancy flux peaks apparent in Figs. 3–5 at cloud top arise from the cloud fraction beginning to fall off significantly at a lower height than the θ_l flux, forcing the buoyancy flux to transition from the wet value toward the more negative dry value.

An inspection of sample 3D fields showed corresponding differences in eddy structures and correlations in the three regimes, supporting the picture we have described: cumulus plumes in a more quiet background

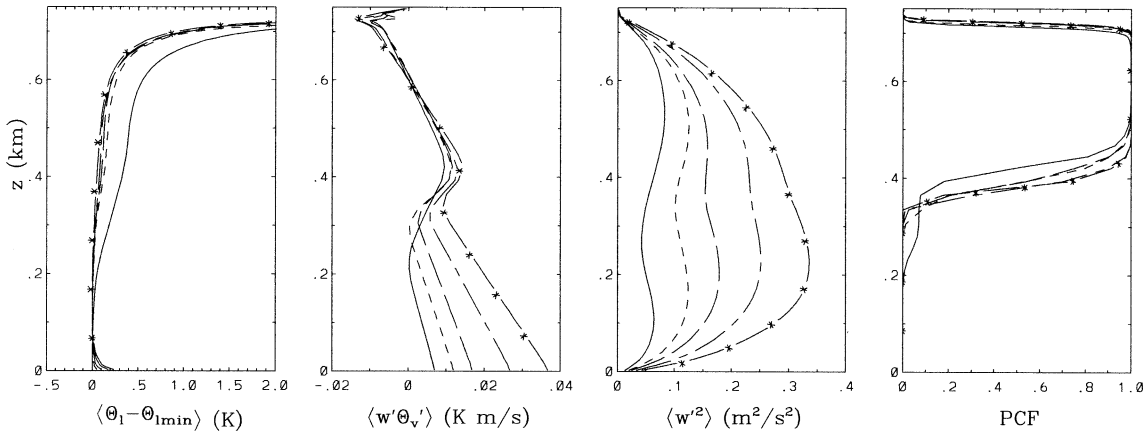

FIG. 4. Mean vertical profiles for selected LES cases with progressively increasing $\overline{w'\theta'_{l0}}$ (runs T0–T4 from Table 1).

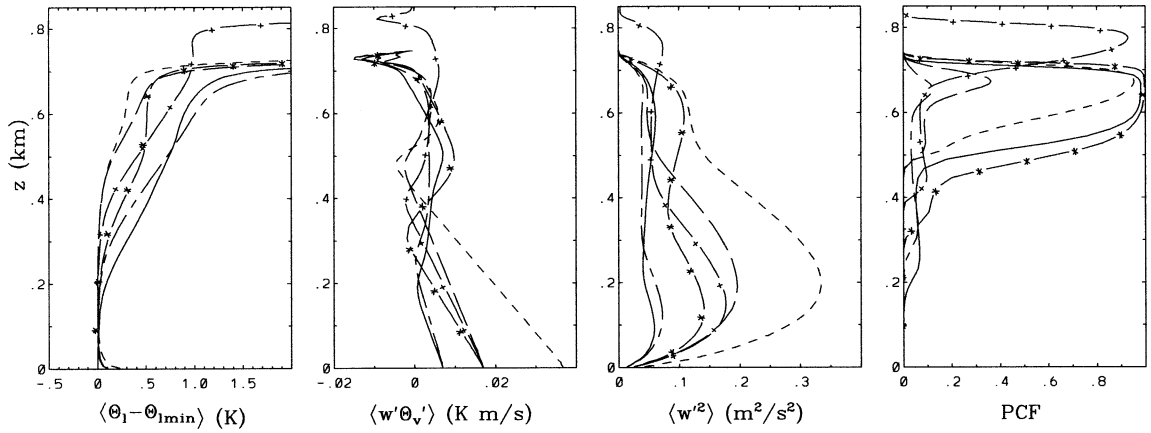

FIG. 5. Mean vertical profiles for selected LES cases in regime III. Runs M1 (solid line), R6 (short dash), R4 (long), R1 (long–short), R8 (*), and NHb (+) from Table 1.

above a weakly capped dry CBL in regime III; classic CBL cellular structure deep in regime I, with the θ_l and q_t fluctuations positively correlated over most of the full layer; an in-between structure in regime II with fewer and stronger plumes in the cloud layer than in regime I (though less organized than in III) and with the θ_l and q_t fluctuations anticorrelated throughout the cloud layer (as in III).

We note in passing two qualitative features of the data in Table 1. Most of the runs with a sizable surface sensible heat flux and no surface latent heat flux are in regime I, as expected, but this does not have to be the case if ζ is large enough, as demonstrated by run C2. Also, there is a strong tendency toward reduced maximum partial cloud fractions in regime III. This arises both from the tendency for higher values of ζ (some large enough to spur CTEI) to push the system into III, and from the increased entrainment and change in cloud structure found in that regime.

c. Convective scaling below cloud base

A key assumption of our analysis is that the subcloud layer in regime III is a simple surface-driven convective boundary layer capped by a weak inversion near cloud base. In LL00 we presented a robust scaling for such layers that collapses the behavior within the mixed layer regardless of the nature of the capping inversion. In Fig. 6 we use this scaling for the selection of regime III profiles from Fig. 5. Characteristic length ($\check{z}$), velocity ($\check{w}$), and buoyancy ($\check{b}$) scales are defined using two robustly measurable parameters in these quasi-steady layers, the surface buoyancy flux ($\overline{wb}_0$), and minus the buoyancy flux slope ($S_b \equiv -d\overline{wb}/dz$): $\check{z} \equiv \overline{wb}_0/S_b$, $\check{w} \equiv (\overline{wb}_0^2/S_b)^{1/3}$, and $\check{b} \equiv (\overline{wb}_0 S_b)^{1/3}$. Given the variation in Fig. 5, the scaling is seen to organize the subcloud data well, and the results are in excellent agreement with the scaled CBL results presented in LL00. It is worth noting that while the simulations in Fig. 6 were all per-

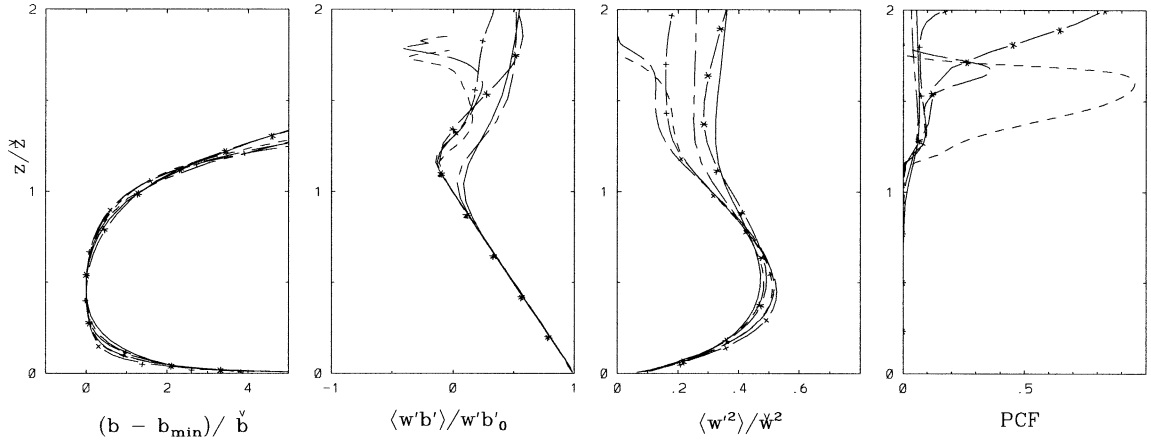

FIG. 6. Mean vertical profiles with subcloud CBL scaling as described in the text for the same cases as in Fig. 5.

formed at comparable spatial resolution, the relative resolution of the subcloud circulations (i.e., $\Delta x/\check{z}$) varies over a large range, and much of the variation remaining in the scaled profiles in Fig. 6 is consistent with what we found for identical dry CBL simulations performed at such different resolutions. The characteristic dynamical buoyancy scale $\check{b}$ is of much smaller magnitude than the buoyancy change at column cloud base; the entire $b - b_{\min}$ profile shown is in the well-mixed layer. Note that regime I and II profiles in the subcloud layer are not collapsed to a universal profile by the same scaling.

d. Decoupling boundary

Equation (18) provides a sharp prediction of the location of the decoupling transition in physical parameter space. In order to test this against our LES results we need a diagnostic for determining whether a given boundary layer is cumulus coupled or not. As described above (and noted by other authors), there are several changes in the layer properties that accompany this transition. Many, such as the growing θ_l and q_t gradients at cloud base or the increase in vertical velocity skewness in the cloud layer, are gradual and do not identify the boundary very sharply. Some, such as a local minimum in the vertical velocity variance profile, do not occur in all cases, or can appear in regime II even well away from the regime III boundary. Here we will use the presence in the mean cloud fraction profile of a column cloud (even if short) below the main cloud base as the signature for the cumulus coupled state. In the cloud fraction profile a local maximum appears near column cloud base when the column clouds are long. When the column clouds are shorter (the column distribution overlapping with the bottom of the main cloud), then the local maximum no longer appears but is replaced by an inflection point. The absence of either signature we take to denote an absence of column clouds. In this determination we work with the measured mean cloud fractions on the points of our vertical grid, and use cubic spline interpolation for points in between so that the features of the profile may be identified with some precision.

We also need prescriptions for determining the quantities in (18) from the LES results. What is required are prescriptions for ''squaring off'' actual profiles to compare with the idealized picture of section 2 (cf. Fig. 1). In the simulations performed with an upper lid there is little ambiguity in the value of z_i; the capping inversion is sharp and there is a clear break in slope in, for example, $\overline{w'\theta_l'}$, within it, where we locate z_i. In those cases with a true inversion, we identify z_i as that height for which the $\overline{w'\theta_l'}$ profile approximated by a constant measured slope in the layer extended to z_i and there discontinuously dropped to zero, has the same integral as the actual measured profile. We advocated this procedure of using robustly measurable quantities such as the flux slope and integral to define z_i, rather than some subtle features within the inversion region, in LL00 and showed that this allows a successful common scaling for weakly and tightly capped CBLs alike. The conserved flux values $\overline{w'\theta_{li}'}$, and $\overline{w'q_{ti}'}$ are determined using the same squaring off procedure by extending the linear slope from the respective profile up to the height z_i.

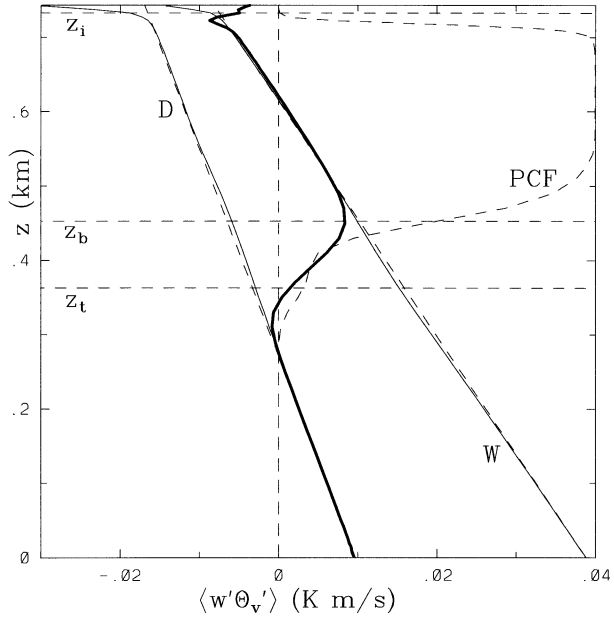

FIG. 7. Measured mean buoyancy flux (heavy line), wet and dry buoyancy fluxes (W and D labeled solid lines), and partial cloud fraction (PCF, dashed) for an intermediate time during run T8 (cf. Fig. 18). Heights determined as described in the text are indicated by horizontal dashed lines; the intersection of the z_i line with the linearized W and D lines (straight dashed) determine the entrainment fluxes W_i and D_i.

For the height of the main cloud base z_b, we use the height at which the mean cloud fraction reaches half its maximum value. We identify a height for the top of the subcloud layer z_c by computing the lifting condensation level of a parcel possessing the mean θ_l and q_t of the bottom half of the subcloud layer. We choose parcel properties from the bottom portion of the layer recognizing that the updrafts on average are slightly moister than their surroundings; the precise fraction chosen has little impact on the height computed because the subcloud layer is so nearly well mixed. We employ this lifting condensation level as well for the layer separation height z_t used in relations for regimes II and III; z_t is not defined for a regime I layer. We will show below (Fig. 12) that this determination of z_t is consistent with the values obtained by assuming a constant entrainment efficiency into the subcloud layer in regime III and using the subcloud scaling of Fig. 6.

Figure 7 illustrates the actual, wet, and dry buoyancy fluxes measured for one sample case, along with the heights z_i, z_b, z_t, and determination of W_i and D_i given by the above procedures. This is a regime III case with

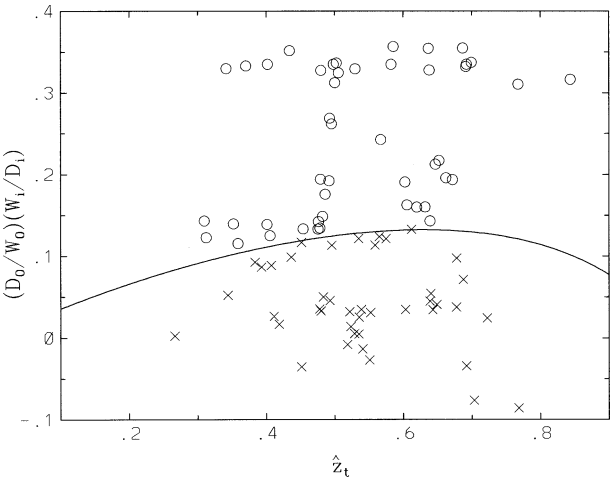

FIG. 8. Results from quasi-steady LES from Table 1 vs the decoupling boundary prediction of Eq. (18). Symbols indicate whether a column cloud is present in the mean cloud fraction profile (crosses) or not (circles).

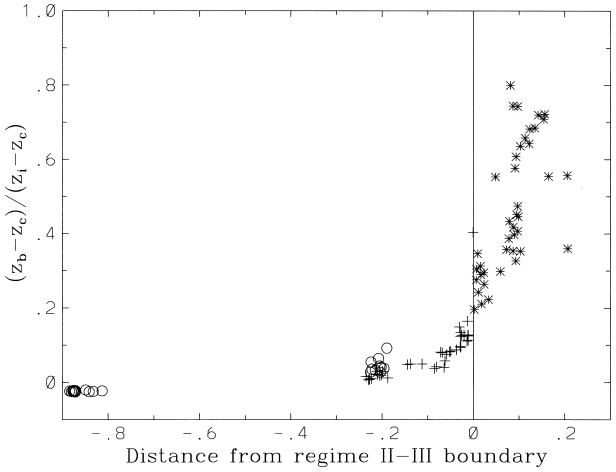

FIG. 9. Relative cloud-base depth from LES data vs distance from predicted decoupling boundary. Symbols indicate data from predicted regimes I (○), II (+), and III (*).

a short column cloud, which raises z_b above z_t by more than it would be in a regime II case. We have intentionally chosen a case here where the layer properties are changing significantly over time (that shown is the middle time in the transitional case of Fig. 18 below) to also illustrate that the conserved fluxes can indeed be linear to a very good approximation even though the thermodynamic profiles are changing with time and not well mixed, if the dynamical eddy timescales are short enough.

With the prescriptions defined we have in Fig. 8 located the LES results on a plot of the left-hand side of (18) versus $\hat{z}_t$, along with the boundary curve defined by (18) (evaluated for $\eta_{sc} = 0.3$ and $\tilde{\eta}_c = 0.5$). Only quasi-steady averages (recognized by approximately linear conserved flux profiles) have been included here. As noted this does not mean that all the cases are steady; some individual simulations with properties such as cloud-base height changing in time each contribute several points to Fig. 8. The different symbols distinguish between cases with column clouds (as indicated by the presence of a local maximum or inflection point in the mean cloud fraction profile below the main cloud) or without. The curve defined by (18) does a good job dividing these two populations. Only one point lies on the ''wrong'' side of the boundary, and it only barely so. There are some regime I points with, as predicted, no column clouds, which lie off scale on this plot well above the decoupling curve. The points with a negative y coordinate lie deep in regime III. For these cases the buoyancy flux at the top of the layer is still negative (along with D_i) but the maximum cloud fractions have dropped well below 1, and W_i is in fact positive.

Figure 9 plots a measure of the relative column cloud depth $[(z_b - z_c)/(z_i - z_c)]$ for each LES data point versus the difference between the right and left sides of Eq. (18) (which gives a measure of the distance from the decoupling boundary). We see that 1) there is little depth to the cloud base on the predicted ''coupled'' side of the parameter space and 2) the column cloud depth on the ''decoupled'' side generally grows with distance from the decoupling boundary.

Figure 10 displays two candidates for decoupling diagnostics, discussed in section 2f, as applied to our LES data. There is a noticeable positive correlation between an increase in either measure, BIR or β, and decoupling (as diagnosed by the presence of column clouds), but no fixed threshold of either does a particularly successful job of diagnosing cumulus coupling overall. We find, for example, some obvious cumulus coupled layers with zero BIR, or clearly well-mixed ones with values of β well above 1; neither measure properly captures the effects of the cloud depth fraction on decoupling.

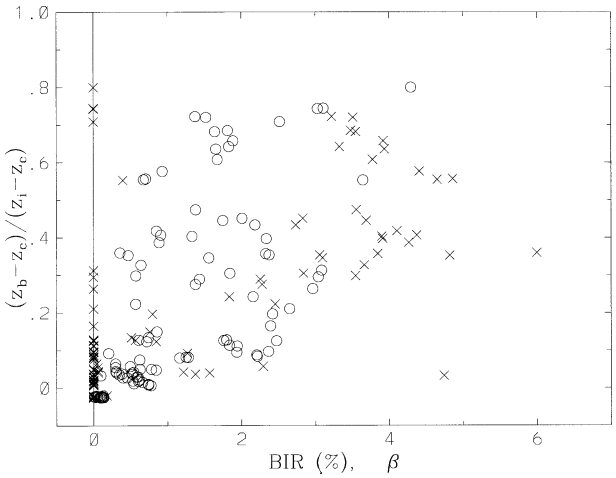

FIG. 10. Other proposed decoupling measures, BIR as in BW97 (×, in percent) and β (○), applied to the LES dataset as discussed in the text.

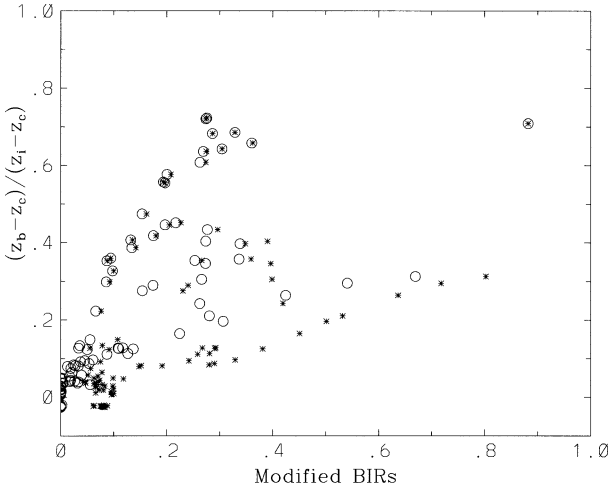

FIG. 11. Two modified BIR measures applied to the LES data: as defined in Stevens (2000; *), and that measure modified to only include negative buoyancy flux below cloud base (○).

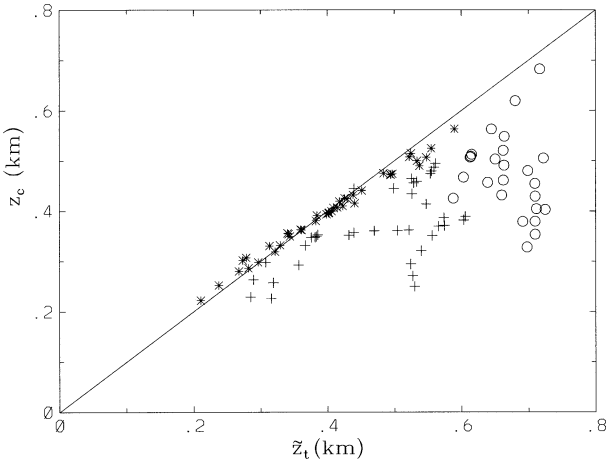

FIG. 12. Measured LES column cloud-base height z_c vs subcloud-layer height from CBL scaling $\tilde{z}_i$. Symbols as in Fig. 9.

Note also that all of the BIR values in the present dataset are well below the 15% threshold for decoupling suggested in BW97. Horizontal averaging of the fluctuations in cloud base reduces the measured BIR. Also the 15% value of BW97 is based in part on results from 2D models, which we would expect to give larger BIRs; we consistently find larger large-eddy entrainment efficiencies (~0.6) in 2D simulations than we find in 3D.

Figure 11 displays two modified versions of the BIR applied to our LES data: that defined in Stevens (2000) and that measure modified to only include negative buoyancy flux below cloud base. Both show a better correlation than the measures of Fig. 10, with the latter of the two performing better than the former. A threshold value of 0.08 for the latter measure divides the dataset into cases with and without column clouds with the fewest exceptions.

e. Entrainment results

We next test whether the entrainment fluxes measured for the LES cases predicted to be in each regime agree with the entrainment prediction for that regime. In regime III we can check both the entrainment rate prediction into the subcloud layer [Eq. (6)] and at cloud top [Eq. (10)]. The consistency of the data with the former can already be inferred from the agreement of the scaled column cloud base heights in Fig. 6. With the scaling used there, the layer height is directly related to the entrainment efficiency $\tilde{z}_t = (1 + \eta_{sc})\tilde{z}$. In Fig. 12 we have plotted z_t as determined from the subcloud lifting condensation level (z_c) versus $\tilde{z}_t$ evaluated with $\eta_{sc} = 0.3$. The agreement between the two is good to ±5% across the regime III data. This agreement is shared by a subset of the regime II points (those near the II–III boundary) with the remainder, and all the regime I points, showing the measured cloud-base height lying below the regime-III-predicted column cloud base, as expected.

Figure 13 displays the cloud-top entrainment rate for the LES results versus the regime III prediction (10). The measured values of D_i/D_0 agree well with those predicted for the subset of the data predicted to be in regime III. The scatter arises only partly from the scatter in Fig. 12; much is due to the conserved flux profiles not being exactly linear, the mean slope below cloud differing modestly from that over the full layer. Figures 14 and 15 show the analogous plots for the regime II and I entrainment predictions, (16) and (12), respectively. As in Fig. 13 the entrainment rates predicted for a given regime correlate well with the measured rates for cases predicted to be within that regime, but poorly with the datasets from the other regimes (some points of which lie off the scale of the given plot). Cases near the predicted II–III or I–II boundaries reasonably satisfy both of the relevant entrainment predictions.

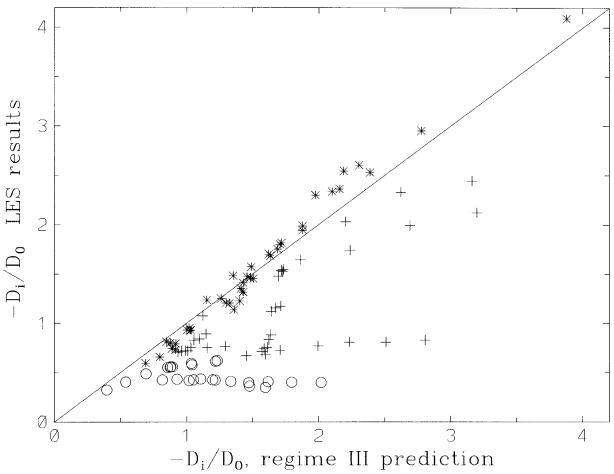

FIG. 13. Normalized entrainment flux from LES results vs regime III prediction (10). Symbols as in Fig. 9.

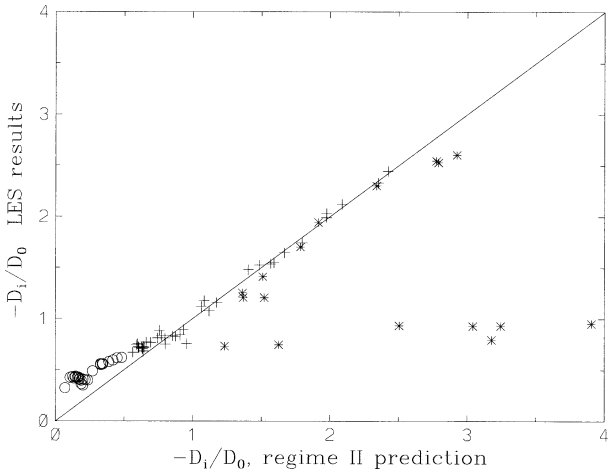

FIG. 14. Normalized entrainment flux from LES results vs regime II prediction (16). Symbols as in Fig. 9.

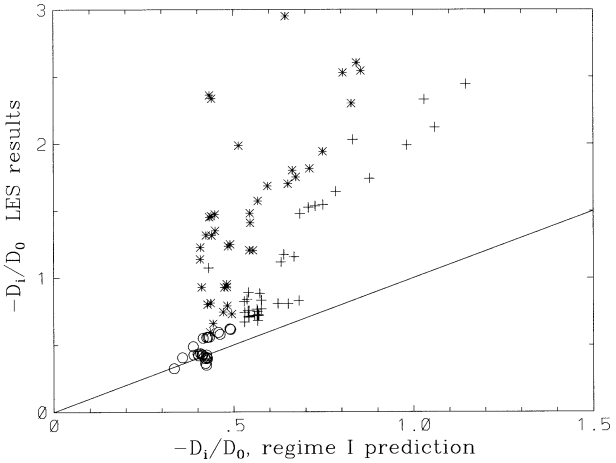

FIG. 15. Normalized entrainment flux from LES results vs regime I prediction (12). Symbols as in Fig. 9.

Figure 16 shows the entrainment results in a different format, computing the corresponding entrainment efficiency for the data in each regime [η_{sc}, η_c, $\tilde{\eta}_c$, η_f, from (6), (7), (17), (9), for data points predicted to be in regimes III, II, II, and I, respectively]. These have been plotted against the difference between the right- and left-hand sides of (18) for convenience, to spread and sort the different cases. The results show a fair scatter but are consistent with the nominal values (0.3, 0.55, 0.5, 0.3, respectively) we have chosen based on data from previous simulations designed to provide more precise measurements of η. Small errors in the determination of quantities such as the heights z_t or z_b or flux slopes lead to larger relative errors in measuring the η's. While perhaps discouraging on the surface, this is ultimately beneficial. In a model we can determine quantities such as the flux slopes, which are of direct importance to the layer dynamics, to a good degree of accuracy even if the η used is not determined to as high an accuracy.

The least successful of the entrainment predictions is that for regime I, but this is not unexpected. In regime III the subcloud circulation (postulated to limit the entrainment rate) is largely universal, as shown in Fig. 6. In regime II the upper circulation has more variation, particularly toward the regime I boundary where the in-cloud plumes may already possess significant vertical momentum at cloud base (from subcloud buoyancy release), which may be responsible for the modest enhancement in entrainment there over that predicted. Nonetheless there is a single basic circulation pattern, and a linear buoyancy flux profile, within the cloud layer in regime II. In regime I, however, the full-layer circulation spans both clear and cloudy regions, the buoyancy flux over the range of the circulation is nonlinear, the liquid water flux may be either positive or negative, and there can be important admixtures of circulations restricted to the cloud or subcloud layers. As regime II is approached a clear enhancement in η_f above 0.3 is seen in the data; values significantly below 0.3 are restricted in the dataset to cases with a significant negative contribution from the liquid water flux.

f. *Transitional cases*

We close by presenting profiles for a few simulations in which the boundary layer transitions between different regimes during the course of the simulation. We noted in section 2d the variety of ways in which a convective layer can transition between regimes II and III as governed by (18). Figure 4 discussed above, while presenting results from a series of simulations rather than a time series from a single one, adequately illustrates for one set of conditions the transition from regime II to III produced by a decrease in D_0/W_0. In run NS1 (Fig. 17), the II–III transition is traversed in a single

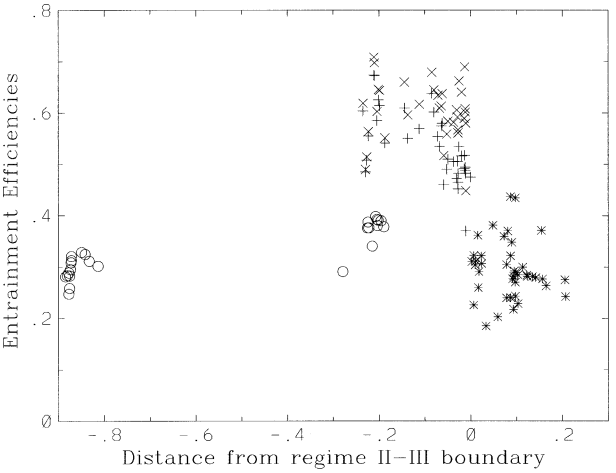

FIG. 16. Large-eddy entrainment efficiencies from LES results vs distance from predicted decoupling boundary: η_f for predicted regime I data (○); η_c (×) and $\tilde{\eta}_c$ (+) for regime II data; η_{sc} for regime III data (*).

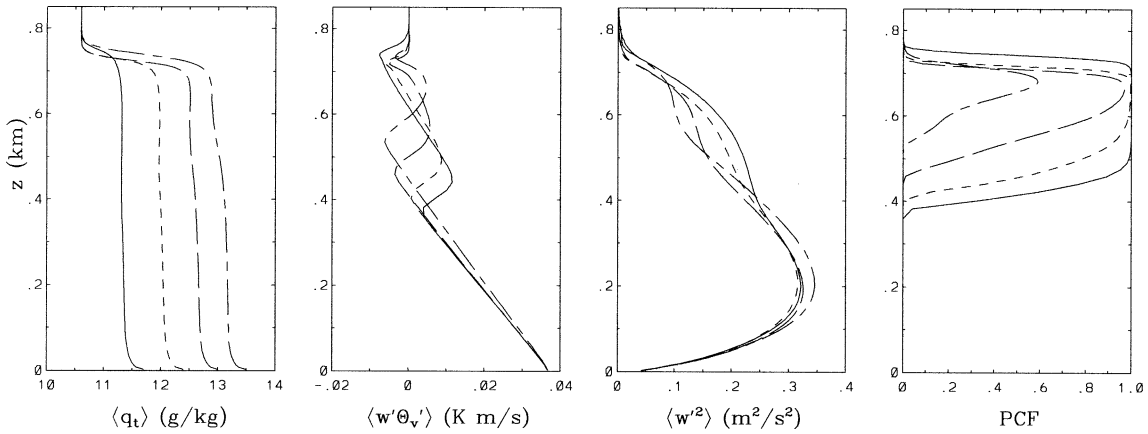

FIG. 17. Sample mean vertical profiles for run NS1, progressing in time from thick cloud to thin.

simulation by the changing cloud-top conditions. As the system evolves W_i/D_i decreases (or, equivalently, ζ increases). The positive surface fluxes heating and moistening the boundary layer increase Δq_t at the inversion while decreasing $\Delta\theta_l$. The decrease in W_i/D_i in this simulation is sufficient to force the transition to regime III even though the decrease in cloud thickness opposes it. The drop in maximum cloud fraction is promoted both by the transition to regime III and by the increase in ζ producing cloud-top conditions that are nominally evaporatively unstable.

In run T8 (Fig. 18) the layer begins in regime II with a very thick cloud. The large-scale advective forcings in this case are such as to continuously reduce the cloud depth. This drives the system first into regime III but later back into II; the column cloud below the main cloud first grows and then shrinks accordingly. In the latter part of this simulation the buoyancy flux is sufficiently small and the rate of decrease in cloud thickness sufficiently large that the system is not in a quasi-steady state; the transition back to regime II is delayed by the time it takes the dynamics to mix out the larger θ_l and q_t gradients formed when the system was in regime III.

4. Concluding remarks

In LL98 we proposed that the cloud-top entrainment rate in a quasi-steady boundary layer represents a property of the large-scale circulations, the limit set by the maximum negative entrainment buoyancy flux the circulation can support. This has much in common with the explanation often given for layer decoupling. In the present work we have treated the two problems, coupled together, on equivalent footing with a single underlying parameterization. Applying the large-eddy entrainment picture to the three idealized eddy scales naturally identified for cloudy boundary layers, led to three idealized behavior regimes defined by which large-scale circulations ultimately limit the cloud-top entrainment rate: ones across the full boundary layer (I), across the cloud layer (II), or across the subcloud layer (III). The agreement found between our LES re-

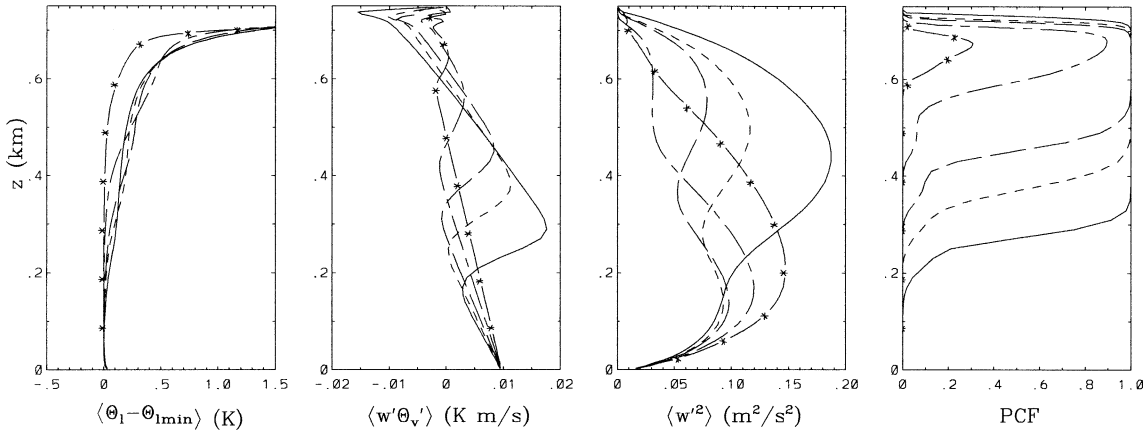

FIG. 18. Sample mean vertical profiles for run T8, progressing in time from thick cloud to thin. The lines represent 2-h averages spaced 4 h apart.

sults and the predictions derived from this picture supports both the applicability of the idealized regimes of section 2 to more realistic layers, and the basic premise of LL98. The predictions tested required only what could be fairly judged as input parameters (i.e., the surface fluxes, cloud-top jump ratio, and cloud-base heights) and involved only two empirical parameters (the entrainment efficiencies for uniform and spot heating cases) with values already determined from previous dry convective boundary layer simulations.

In each regime we derived a prediction for the entrainment flux at cloud top that was found to be in good agreement with our LES results. The boundary between regimes II and III we identified with the decoupling transition leading to a cumulus coupled layer. When the layer is driven only by surface fluxes, our prediction for this boundary [Eq. (18)] is solely a function of the normalized layer separation height $\hat{z}_t$ and a simple product of surface and cloud-top flux ratios. This prediction was also found to be in excellent agreement with the LES results. When cloud-top radiative cooling is included, the prediction for the decoupling boundary [Eq. (A4)] is correspondingly more complex. In general decoupling is promoted by an increase in surface latent heat flux, decrease in surface sensible heat flux, or increase in ζ, the cloud-top moisture-to-temperature jump ratio. It may be either promoted or retarded by an increase in the cloud thickness or radiative flux jump, depending on $\hat{z}_t$, ζ, and the fraction α of the radiative flux jump that drives large-scale circulations. Layers can evolve from well mixed to decoupled in several natural ways, easily realized in LES results, for example, by gradual decrease in surface Bowen ratio, increase in cloud thickness, or increase in ζ as a layer warms and moistens.

While we have not stressed it in this work, understanding the decoupling transition in physical parameter space has important implications for understanding the breakup of horizontally uniform cloud sheets. The growth of column clouds in regime III is partly achieved by a decrease in the main cloud depth, which tends to break up the cloud deck. This breakup is enhanced by large values of ζ (such as are required for cloud-top entrainment instability) but does not require them. The apparent complexity of the decoupling boundary may be in part responsible for the failure of any simple criterion so far proposed to predict stratus cloud breakup for the wide variety of conditions encountered.

There are several clear avenues for improving and extending the present work. The class of boundary layers we have considered most completely is an important but limited one: those that are quasi steady and driven solely by surface fluxes. This is sufficient for many realizations of shallow cumulus and probably for the decoupling transition encountered in wintertime cold air outbreaks (a case noted in BW97), but for many other instances radiative cooling or warming play a significant role. We have included radiative cooling at cloud-top in the treatment in appendix A; a systematic test of those predictions against LES results would be worthwhile. We have not done so to date in part because of the lack of a satisfactory way to predict (or even cleanly diagnose) α; progress on that front is clearly needed. At the cost of yet more complexity, we could straightforwardly include in our analysis any fixed radiative flux profile (or other forcing such as precipitation) and treat, for example, diurnal decoupling on a similar footing.

We have defined regimes I and II in the simple approximation in which either the full-layer or cloud-layer circulation is clearly dominant. In some cases, treating the dynamics as a more even mixture of the two might be more appropriate. In addition, the effects of radiation on the transition between these regimes should be addressed, along with clarifying under what conditions the structure of the in-cloud circulation transitions from one with a high entrainment efficiency to one with a lower efficiency.

Finally, there is a need for modeling the mean buoyancy flux in terms of the mean conserved fluxes of heat and moisture for partly cloudy, highly skewed conditions such as shallow cumulus. Cloud-top entrainment provides an important feedback in determining the circulation structure and resulting buoyancy flux, so the picture we have presented here may prove useful in addressing this long-standing problem. A successful buoyancy flux model for these cases would allow us to apply an entrainment efficiency condition for the upper circulation in addition to that for the subcloud circulation in regime III. This extra condition could be used to solve for an additional property in quasi-steady state, for example, the column cloud base height or maximum partial cloud fraction. In addition it would allow a more complete treatment of unsteady layer dynamics in which the upper and lower circulations have not equilibrated.

Acknowledgments. This work was supported by Grant N00014-98-1-0595 from the Office of Naval Research with R. Ferek as technical monitor. Review comments of C. Bretherton, D. Lilly, and B. Stevens led to significant improvements in the presentation. D. L. would also like to thank members of the GCSS Working Group 1 for useful discussions.

APPENDIX A

A More Complete Solution for the Decoupling Boundary

We begin by comparing, in Fig. A1, the decoupling boundary as given in (18) with results from the complete system of Eqs. (6)–(8) in order to justify the approximation leading to (18). The full solution is a weak function of W_i/D_i; curves are shown for three values (0, 0.25, 0.5) spanning a representative range. Given the simplification gained, the approximate solution of (18) is seen to do a good job of representing the full solution.

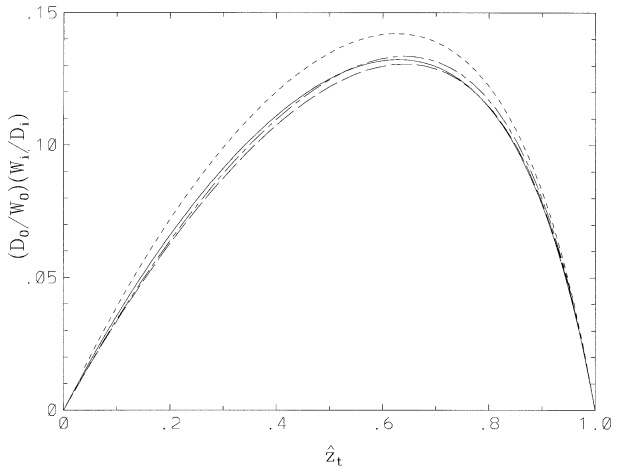

FIG. A1. The decoupling boundary from (18) (solid line) compared with the full solution from (6)–(8) for $W_i/D_i = 0$ (short dash), 0.25 (short–long dash), 0.5 (long dash), using the nominal values: $\eta_{sc} = 0.3$, $\eta_c = 0.55$, $\tilde{\eta}_c = 0.5$, $\eta_b = 0.3$.

We proceed to solve for the decoupling boundary at this level of approximation with a radiative flux divergence included in a thin layer at cloud top. The computation is analogous to that given in section 2, but with additional complications. First, W_i/D_i is no longer a function of ζ alone, as in (5), but depends on the entrainment rate itself. Accordingly we should phrase our solution in terms of ζ instead of W_i/D_i despite the added complexity. In our simple jump approximation the conserved moisture flux at z_i is still given by the entrainment contribution alone ($\overline{w'q'_{ti}} = -w_e\Delta q_t$), but the θ_l flux now includes a contribution from ΔF_r, the total radiative flux jump at cloud top ($\overline{w'\theta'_{li}} = \Delta F_r - w_e\Delta\theta_l$). Eliminating the entrainment velocity w_e from these relations, rearranging, and using the definitions of ζ, W_i, and D_i gives the replacement for Eq. (5):

$$\frac{W_i}{D_i} - \frac{\Delta F_r \phi}{D_i} = \frac{(X_1^w - X_2^w\zeta)}{(1 - X_2^d\zeta)} \equiv \chi, \qquad \text{(A1)}$$

where

$$\phi \equiv \zeta(X_2^w - X_1^w X_2^d)/(1 - X_2^d\zeta). \qquad \text{(A2)}$$

Second, the large-eddy entrainment efficiency for the cloud circulation [replacing (7)] now includes a contribution from that fraction, $\alpha\Delta F_r$, of the radiative flux jump which buoyantly drives large-scale circulations (LL98):

$$\eta_c = (X_1^w\alpha\Delta F_r - W_i)/(W_b + X_1^w\alpha\Delta F_r). \qquad \text{(A3)}$$

By including radiation the number of parameters governing our problem has increased by 2 since the full ΔF_r appears in the cloud-top jump conditions (22) but only a fraction $\alpha\Delta F_r$ in η_c. The difference between the two, $(1 - \alpha)\Delta F_r$, represents cooling that does not lead to negatively buoyant parcels driving large-scale circulations—either because the radiation originates from parcels in the stable layer at the base of the inversion (which includes some of the cloud top), or because small-scale (e.g., shear generated) turbulence mixes the negatively buoyant, radiatively cooled parcels with warmer inversion air before they have a chance to descend. The interpretation and treatment of this ''direct cooling'' portion of ΔF_r (as we called it in LL98) has been a subject of debate in the literature. In our opinion, a completely satisfactory treatment is still lacking. While some have interpreted the effect as arising purely from horizontal averaging over a nonuniform cloud top and have tried to parameterize it accordingly (e.g., Moeng et al. 1999), we would argue that a potentially significant effect remains even for horizontally homogeneous conditions, with the magnitude dependent on the local thermodynamic gradients, radiative flux profile, and mixing rates. No attempt is made to solve the problem here; α is treated as an independent parameter specified externally. We note, however, that deep in regime II or in regime III, there will be a tendency for α to be reduced because of the enhanced degree of stability in the profiles in the upper part of the layer in these regimes, so that for small $\Delta F_r/W_b$, $\alpha = 0$ is probably a good approximation near the II–III boundary.

To essentially the same level of approximation as given in (18), the criterion for decoupling now becomes

$$\frac{D_0}{W_0}\chi \le \hat{z}_t \frac{(1 - \hat{z}_t)\tilde{\eta}_c - [X_1^w\alpha(1 - \tilde{\eta}_c) - (1 + \hat{z}_t\tilde{\eta}_c)\phi]\dfrac{\Delta F_r}{W_0}}{(1 + \hat{z}_t\tilde{\eta}_c)(1 + \eta_{sc} - \hat{z}_t)}. \qquad \text{(A4)}$$

This reduces to (18) in the limit $\Delta F_r \to 0$. Again it is straightforward, but quite messy, to find the full solution following from Eqs. (A1), (A3), (6), and (8). The results are compared with those from the approximation (A4) in Fig. A2 for a relatively large level of radiative cooling and selected values of α and ζ, supporting the validity of the simpler approximation.

The coefficient of ΔF_r in (A4) can take either sign, meaning that an increase in ΔF_r can either promote or inhibit decoupling depending on α, ζ, and $\hat{z}_t$. There are two competing effects, most easily illustrated by two simple limits. When $\zeta = 0$ (no q_t jump) and $\alpha \neq 0$, then an increase in ΔF_r tends to cool the cloud layer, reducing the temperature jump at cloud base (if one is

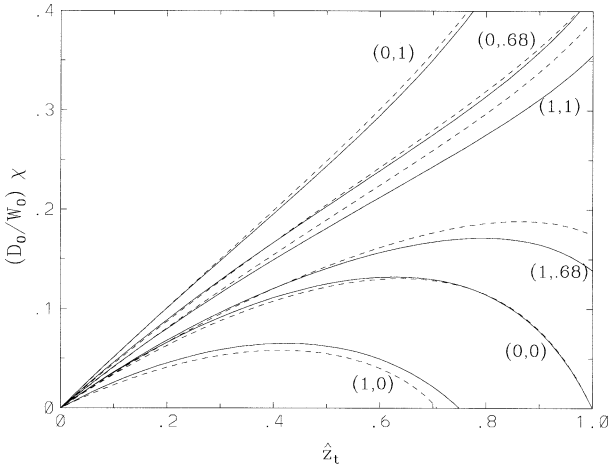

FIG. A2. The decoupling boundary from (A4) for $\Delta F_r/W_0 = 0.5$ (solid lines) compared with the full solution from (A1), (A3), (6), (8) (dashed lines). The pairs of curves are plotted for the values of (α, ζ) as labeled. Note that the curve for $(\alpha = 0, \zeta = 0)$ is equivalent to that for $\Delta F_r = 0$.

present), and helping to drive the subcloud transport (if the system is coupled), thus inhibiting layer decoupling. If $\alpha = 0$ (all direct cooling limit) and $\zeta \neq 0$, then Eq. (A3) reduces to (7) and Eq. (18) still represents the decoupling boundary; the only effect of a nonzero ΔF_r is in Eq. (A1) where it modifies the relation between the cloud-top jump conditions and the flux ratio W_i/D_i. In this limit an increase in ΔF_r has the same effect as an increase in ζ, promoting decoupling in the same way by enhancing entrainment drying and the in-cloud buoyancy flux. With both effects present, an increase in ΔF_r will promote decoupling if $\zeta > \zeta_{\text{crit}}$ or inhibit it if $\zeta < \zeta_{\text{crit}}$, where

$$\zeta_{\text{crit}} = \frac{X_1^w \alpha(1 - \tilde{\eta}_c)}{X_2^w(1 + \hat{z}_t\tilde{\eta}_c) - X_1^w X_2^d[1 - \alpha(1 - \tilde{\eta}_c) + \hat{z}_t\tilde{\eta}_c]}. \tag{A5}$$

We caution that when $\alpha > 0$, we have yet to quantitatively specify how η_c will respond to changes in the structure of the turbulence in the cloud as cloud-top radiative flux divergence becomes comparable or larger than cloud-base buoyancy flux. When the turbulence is no longer dominated by latent driven plumes, η_c may be expected to drop from $\sim$0.6 to $\sim$0.3, affecting the decoupling boundary. Thus the solution in (A4) with $\tilde{\eta}_c \approx 0.5$ should be viewed as valid up to some modest values of $\alpha\Delta F_r/W_b$, but not indefinitely.

APPENDIX B

Table of Simulations

TABLE B1. Principal simulations. Those with an "N" in the run label were performed with a true inversion, all others with a sharp inversion under a fixed lid; the surface latent heat flux $\overline{w'q'_{t0}}$ was 4×10^{-5} g g^{-1} m s^{-1} for all cases except those with a "C" in the run label, for which it was zero; all simulations were performed with a uniform 40-m horizontal grid spacing except for those with an "H" in the run label, performed at 20-m resolution; there was no large-scale subsidence included except in runs NS1 (uniform divergence of -8.5×10^{-6}) and NS2 (-5.33×10^{-6}). The surface sensible heat flux $\overline{w'\theta'_{l0}}$ (in K m s^{-1}), cloud-top jump ratio ζ, surface dry-to-wet buoyancy flux ratio D_0/W_0, inversion wet-to-dry buoyancy flux ratio W_i/D_i, nondimensional column cloud-base height $\hat{z}_c$ ($=\hat{z}_t$, the layer separation height in regimes II and III), and inversion to surface dry buoyancy flux ratio $-D_i/D_0$ are as defined in the text; $(d\theta_l/dt)_{\text{LS}}$ (in K h^{-1}) and $(dq_t/dt)_{\text{LS}}$ (in g kg^{-1} h^{-1}) are imposed uniform large-scale heating and moistening terms; pcf is the maximum mean partial cloud fraction; and R is the nominal regime the boundary layer is classified in according to the analysis of section 2. All output quantities are averages over the simulation segment used unless there was significant time development during the period, in which case the range spanned by the set of 2-h averages is given.

Run	$\overline{w'\theta'_{l0}}$	$\left(\frac{d\theta_l}{dt}\right)_{\text{LS}}$	$\left(\frac{dq_t}{dt}\right)_{\text{LS}}$	ζ	$\frac{D_0}{W_0}$	$\frac{W_i}{D_i}$	$\hat{z}_c$	pcf	$-\frac{D_i}{D_0}$	R
N1	0.0	0.0	0.0	1.3	0.20	0.012	0.27	0.86	4.1	III
R1	0.0	0.0	−0.108	1.7	0.18	−0.19	0.45	0.12	1.99	III
R2	0.0	0.0	−0.108	1.0	0.19	0.1	0.41	0.62	2.35	III
M1	0.0	0.0	−0.108	0.58	0.19	0.28	0.34	0.98	2.95	III
NHb	0.01	0.0	0.0	1.4	0.43	−0.02	0.52	0.93	1.45	III
Nb	0.01	0.0	0.0	1.24	0.42	0.02	0.52	0.94	1.47	III
R4	0.01	−0.048	−0.108	1.6	0.39	−0.15	0.69	0.34	0.81	III
R5	0.01	−0.048	−0.108	1.0	0.40	0.10	0.65	0.82	0.93	III
R6	0.03	−0.096	0.0	1.1	0.71	0.1	0.68	0.95	0.77	III
M2	0.01	−0.048	−0.108	0.53	0.40	0.30	0.56	1.0	1.21	III
M3	0.02	−0.096	−0.108	0.57	0.57	0.28	0.62	1.0	0.87	II
R7	0.02	−0.048	0.0	1.1	0.57	0.08	0.64	0.96	0.94	III
R8	0.01	−0.072	0.0	1.1	0.42	0.08	0.60–0.48	1.0	1.2–1.8	III
NS1	0.03	0.0	0.0	0.4–1.6	0.75	0.34–(−0.11)	0.57–0.77	1.0–0.6	0.77–0.60	II–III
NS2	0.01	0.0	0.0	1.1–1.5	0.42	0.08–(−0.06)	0.54	0.95–0.38	1.35–1.14	III
T0	0.0	0.025	−0.108	0.0	0.19	0.49	0.41	1.0	2.5	III
T1	0.005	0.0	−0.108	0.05	0.30	0.47	0.48	1.0	1.52	II
T1b	0.005	0.0	0.0	0.06	0.30	0.46	0.45–0.31	1.0	1.7–2.1	II

TABLE B1. (*Continued*)

Run	$\overline{w'\theta_{l0}'}$	$\left(\frac{d\theta_l}{dt}\right)_{LS}$	$\left(\frac{dq_t}{dt}\right)_{LS}$	ζ	$\frac{D_0}{W_0}$	$\frac{W_i}{D_i}$	$\hat{z}_c$	pcf	$-\frac{D_i}{D_0}$	R
T2	0.01	0.0	−0.108	0.0	0.38	0.50	0.49	1.0	1.15	II
T3	0.02	−0.096	−0.108	0.04	0.55	0.48	0.50	1.0	0.86	II
T4	0.03	0.0	0.0	0.05	0.70	0.47	0.50	1.0	0.73	II
T5	0.03	−0.16	0.0	0.1	0.72	0.46	1.0–0.48	0.0–1.0	0.33–0.73	I–II
Nd	0.03	0.0	0.0	0.04	0.70	0.48	0.50	1.0	0.76	II
NHd	0.03	0.0	0.0	0.1	0.72	0.43	0.50	1.0	0.68	II
N2	0.04	0.0	−0.072	0.17	0.85	0.42	0.59–0.69	1.0	0.62–0.56	I
T6	0.03	0.0	0.0	0.06	0.74	0.45	0.69	1.0	0.56	I
C1	0.03	−0.096	0.0	0.05	2.1	0.47	0.59–0.72	1.0	0.43	I
CNH	0.03	−0.097	0.0	0.0	2.0	0.49	0.51	1.0	0.36	I
CN	0.03	−0.097	0.0	0.0	2.0	0.49	0.43–0.64	1.0	0.4–0.44	I
C2	0.03	−0.096	0.192	1.0	2.1	0.10	0.66	1.0	0.72	II
T8	0.0025	0.0	−0.216	0.0	0.25	0.5	0.31–0.84	1.0–0.31	2.4–0.53	II–III–II

REFERENCES

Bretherton, C. S., and M. C. Wyant, 1997: Moisture transport, lower-tropospheric stability, and decoupling of cloud-topped boundary layers. *J. Atmos. Sci.,* **54,** 148–167.

——, and Coauthors, 1999: An intercomparison of radiatively driven entrainment and turbulence in a smoke cloud as simulated by different numerical models. *Quart. J. Roy. Meteor. Soc.,* **125,** 391–423.

Brown, A. R., 1999: The sensitivity of large-eddy simulations of shallow cumulus convection to resolution and subgrid model. *Quart. J. Roy. Meteor. Soc.,* **125,** 469–482.

Cuijpers, J. W. M., and P. G. Duynkerke, 1993: Large-eddy simulation of trade-wind cumulus clouds. *J. Atmos. Sci.,* **50,** 3894–3908.

de Roode, S. R., and P. G. Duynkerke, 1997: Observed Lagrangian transition of stratocumulus into cumulus during ASTEX: Mean state and turbulence structure. *J. Atmos. Sci.,* **54,** 2157–2173.

Deardorff, J. W., 1980: Cloud top entrainment instability. *J. Atmos. Sci.,* **37,** 131–147.

Garstang, M., and A. K. Betts, 1974: A review of the tropical boundary layer and cumulus convection: Structure, parameterization, and modeling. *Bull. Amer. Meteor. Soc.,* **55,** 1195–1205.

Grant, A. L. M., and A. R. Brown, 1999: A similarity hypothesis for shallow cumulus transports. *Quart. J. Roy. Meteor. Soc.,* **125,** 1913–1936.

Kraus, H., and E. Schaller, 1978: A note on the closure in Lilly-type inversion models. *Tellus,* **30,** 284–288.

Krueger, S. K., G. T. McLean, and Q. Fu, 1995: Numerical simulation of stratus-to-cumulus transition in the subtropical marine boundary layer. Part I: Boundary layer structure. *J. Atmos. Sci.,* **52,** 2839–2850.

Lewellen, D. C., and W. S. Lewellen, 1998: Large-eddy boundary layer entrainment. *J. Atmos. Sci.,* **55,** 2645–2665.

——, and ——, 2000: Boundary layer entrainment for different capping conditions. Preprints, *14th Symp. on Boundary Layers and Turbulence,* Aspen, CO, Amer. Meteor. Soc., 80–83.

——, ——, and S. Yoh, 1996: Influence of Bowen ratio on boundary layer cloud structure. *J. Atmos. Sci.,* **53,** 175–187.

Lock, A. P., 1998: The parameterization of entrainment in cloudy boundary layers. *Quart. J. Roy. Meteor. Soc.,* **124,** 2729–2753.

——, and M. K. MacVean, 1999: The parameterization of entrainment driven by surface heating and cloud-top cooling. *Quart. J. Roy. Meteor. Soc.,* **125,** 271–300.

——, A. R. Brown, M. R. Bush, G. M. Martin, and R. N. B. Smith, 2000: A new boundary layer mixing scheme. Part I: Scheme description and single-column model tests. *Mon. Wea. Rev.,* **128,** 3187–3199.

Mellor, G. L., 1977: The Gaussian cloud model relations. *J. Atmos. Sci.,* **34,** 3161–3169.

Moeng, C.-H., 2000: Entrainment rate, cloud fraction, and liquid water path of PBL stratocumulus clouds. *J. Atmos. Sci.,* **57,** 3627–3643.

——, P. P. Sullivan, and B. Stevens, 1999: Including radiative effects in an entrainment-rate formula for buoyancy driven PBLs. *J. Atmos. Sci.,* **56,** 1031–1049.

Randall, D. A., 1980: Conditional instability of the first kind, upside down. *J. Atmos. Sci.,* **37,** 125–130.

Siebesma, A. P., and J. W. M. Cuijpers, 1995: Evaluation of parametric assumptions for shallow cumulus convection. *J. Atmos. Sci.,* **52,** 650–666.

Sommeria, G., 1976: Three-dimensional simulation of turbulent processes in an undisturbed trade-wind boundary layer. *J. Atmos. Sci.,* **33,** 216–241.

——, and J. W. Deardorff, 1977: Subgrid-scale condensation in models of nonprecipitating clouds. *J. Atmos. Sci.,* **34,** 344–355.

Stage, S., and J. Businger, 1981: A model for entrainment into a cloud-topped marine boundary layer. Part I: Model description and application to a cold-air outbreak episode. *J. Atmos. Sci.,* **38,** 2213–2229.

Stevens, B., 2000: Cloud transitions and decoupling in shear-free stratocumulus-topped boundary layers. *Geophys. Res. Lett.,* **27,** 2557–2560.

——, and Coauthors, 2001: Simulations of trade wind cumuli under a strong inversion. *J. Atmos. Sci.,* **58,** 1870–1891.

Stevens, D., and C. S. Bretherton, 1999: Effects of resolution on the simulation of stratocumulus entrainment. *Quart. J. Roy. Meteor. Soc.,* **125,** 425–439.

Sykes, R. I., and D. S. Henn, 1989: Large-eddy simulation of turbulent sheared convection. *J. Atmos. Sci.,* **46,** 1106–1118.

——, W. S. Lewellen, and D. S. Henn, 1990: Numerical simulation of the boundary layer eddy structure during the cold-air outbreak of GALE IOP-2. *Mon. Wea. Rev.,* **118,** 363–374.

Turton, J. D., and S. Nicholls, 1987: Diurnal variation of stratocumulus. *Quart. J. Roy. Meteor. Soc.,* **113,** 969–1009.

van Zanten, M. C., P. G. Duynkerke, and J. W. M. Cuijpers, 1999: Entrainment parameterization in convective boundary layers derived from large eddy simulations. *J. Atmos. Sci.,* **56,** 813–828.

Wyant, M. C., C. S. Bretherton, H. A. Rand, and D. E. Stevens, 1997: Numerical simulations and a conceptual model of the subtropical marine stratocumulus to trade cumulus transition. *J. Atmos. Sci.,* **54,** 168–192.